

Rijksuniversiteit
Groningen

Faculteit der Wiskunde en Natuurwetenschappen
Technische Natuurkunde

July 12, 2010

Spin Transport in Few Layer Graphene Field Effect Transistors

by: Fasil Kidane Dejene



rijksuniversiteit
groningen

Research Group: Physics of Nanodevices

Group Leader: Prof. dr. ir. B. J. van Wees

Supervisor: drs. Thomas Maaßen

Referent: Dr. Tamalika Banerjee

Period: September 2009 - July 2010

Acknowledgements

I have to thank a lot of people whose support was invaluable during the time of my master project. Special thanks go to Prof. dr. ir. Bart J. van Wees for offering me the opportunity to work in his ever growing group. I would very much like to thank Drs. Thomas Maaßen for supervising me, teaching me and answering my naive questions. Also special thanks go to the whole graphene team for all the hand you lent me during measurements and device processing. I can not thank you enough. I also want to thank Ass.prof. Tamalika Banerjee for taking her time to read my thesis. Last but not least I would like to thank all FND group members. There was always somebody who can help if there was a technical problem or if I had a question. It was a really great year in a very good group and I learned many new things. Of course, that was one of the reasons why I chose this group for my PhD which I am eagerly awaiting to start.

Abstract

We studied electronic spin transport in few layer graphene (FLG) spin valve devices of various number of layers ranging from 5 to 17. The spin diffusion coefficient and spin life time are found to depend on the number of layers of graphene. The spin life time was observed to increase monotonically with number of layers where as the spin diffusion coefficient shows the opposite behavior. With in the nearest neighbor tight binding calculation of bilayer graphene we used a unified zone folding scheme to explain our FLG results in terms of effective bilayers and a single graphene layer. The results were used to obtain the density of states of FLG from which charge diffusion coefficients in FLG are calculated using Einstein's relation. From a linear scaling between spin relaxation length and the diffusion coefficient we confirm that the Elliot-Yafet mechanism is the most dominant relaxation mechanism in FLG systems. Comparison of charge and spin diffusion coefficients show that transport is limited by impurity potential scattering. This is also reflected by the long spin life times in FLG systems due to the effect of screening of charges in the very lower lying layers.

Contents

1	Introduction to spintronics in few layer graphene	1
1.1	Spintronics	1
1.2	Motivation for FLG spintronics	2
1.3	Outline	3
2	Theory	5
2.1	Electronic properties of FLG	5
2.1.1	Single layer graphene, bilayer graphene and few layer graphene	5
2.1.2	Zone folding scheme	9
2.1.3	Screening in few layer graphene	11
2.2	Spin transport in few layer graphene	11
2.2.1	Electrical spin injection and accumulation	12
2.2.2	Detection of spin transport	14
2.2.3	Conductivity mismatch and role of contacts	16
2.2.4	Spin relaxation in graphene and FLG	16
2.2.5	Hanle spin precession in FLG	17
3	Experimental	19
3.1	Device preparation	19
3.1.1	Deposition of few layer graphene flakes	19
3.1.2	Selecting FLG flakes	20
3.1.3	Determination of number of layers	21
3.1.4	AlO _x deposition	22
3.1.5	Contact design and electron beam lithography (EBL)	22
3.1.6	Ferromagnetic metal electrode deposition	25
3.1.7	Lift-off and wire bonding	25
3.2	Measurement setup	26

CONTENTS

4	Measurements	29
4.1	Charge transport measurements	29
4.2	Spin transport measurements	32
4.2.1	Spin valve measurement	32
4.2.2	Hanle spin precession measurement	34
4.2.3	Gate dependent spin precession measurement	36
5	Conclusions	39
A	Device fabrication recipe for FLG spintronic devices	41
A.1	FLG deposition	41
A.2	FLG flake selection & characterization	42
A.3	Tunnel barrier deposition and EBL	42
	References	49

Chapter 1

Introduction to spintronics in few layer graphene

1.1 Spintronics

An electron has an intrinsic spin in addition to its charge. In electronics charge is used a fundamental entity for solid state device applications. In spintronics, though, the intrinsic spin of an electron besides the electronic charge is used. Researches in spintronics have provided us with fast and efficient memory elements that we currently use in our PCs. The 2007 Nobel Prize in Physics has indeed its root to this fundamental behavior of the electron. It was awarded to Peter Grünberg and Albert Fert for the discovery of giant magnetoresistance (GMR) effect [1, 2]. In their work, they independently showed that the electrical resistance measured across magnetic layers spatially separated by a non-magnetic metallic spacer exhibits two resistance states that mainly depends on the relative orientation of the magnetization directions of the ferromagnets (FM). In the parallel orientation, when both magnetization of the layers point in the same direction, a low resistance state is measured as a result of electrons undergoing less spin dependent scattering events. On the other hand they go through a relatively high spin dependent scattering events when the ferromagnetic layers are aligned anti parallel to each other resulting in a high resistance state. Past and present memory devices used in hard disks of our computers would not have been possible with out the two states '0' and '1' equivalent to the high resistance and low resistance states as mentioned above. The discovery of GMR effect led to the proposal of the Datta-Das spin field effect transistor (sFET) [3]. The sFET requires spin injection from the source,

transport through the channel where spin orientation can be influenced by the gate and spin detection at the drain contact. For this, a material with high spin orbit coupling is required. So far it is not possible to monitor spin transport along the channel by an external gate voltage. Electrical spin injection into metallic systems [4, 5], semiconductors [6, 7] and most recently into graphene [8, 9, 10] has been demonstrated successfully. Spin injection in to semiconductors from FMs is problematic compared to their metallic counterparts. This is because unlike the ohmic FM/Metallic interface at the FM/semiconductor interface forms a Schottky barrier that has to be overcome for efficient injection resulting in the conductivity mismatch problem [11]. As the name implies it arises due to large conductivity mismatch (difference) between the ferromagnet and semiconductors [12]. It was solved by injecting electrons to go through a tunnel barrier before they enter into the semiconductor [11, 13].

Most of these measurements employed the Johnson-Silisbee non-local detection technique to verify spin transport in non magnetic materials. In this technique the path of electron charge current is separated from the spin transport path thereby allowing to detect and measure spin signals from the source. This technique unambiguously confirms spin transport from injector to detector by excluding other spin related effect like Hall effect and other magneto resistance effects [4, 5, 8].

1.2 Motivation for FLG spintronics

Recently this same technique is used to detect spin transport in graphene [8, 9, 14]. Graphene is a one atomic thick sheet of carbon atoms arranged in a hexagonal structure. Currently it has attracted lots of interest in electronics and spintronics owing to its unique electrical, thermal, mechanical and structural properties. High mobility of charge carriers [15, 16], low spin-orbit and hyperfine interactions [17, 18] that resulted in spin relaxation lengths of up to $2\mu\text{m}$ [8] and most importantly the ease of gate tunability are few aspects why graphene is becoming popular in current spintronics researches. Since the first graphene spin-valve devices, numerous important understandings of spin transport in graphene has been reported [19, 20]. By comparing charge and spin diffusion coefficients, linear scaling between momentum and spin scattering is obtained as evidence for the dominance of the Elliot-Yafet (EY-) spin scattering [21] where momentum scattering plays an important role. Since graphene

is deposited on a substrate, impurities sitting at the graphene/SiO₂ substrate are probably main contributors to spin scattering. Getting rid off substrate induced impurities spin relaxation length as high as 10 μ m is envisioned [14].

In suspended graphene [22, 23, 24] based spin-valve devices the graphene sits few hundred nm above the substrate and spin transport will not be affected by impurity scattering from the substrate. These types of devices will definitely have the answers as to how spin information is lost in graphene apart from the EY mechanism. However, from device preparation point of view it is difficult to make ferromagnetic contacts on suspended graphene and perform spin transport measurements. For the time being we study few layer graphene (FLG) based spin valves to understand to what extent substrate induced impurities influence spin transport and meanwhile understand the effect of screening of charges on the spin transport. Since the Elliot Yafet spin relaxation is the most dominant one and occurs from momentum scattering from impurities [21], screening of these impurities in FLG system should in principle increase the lifetimes of spins. Here we try to study spin transport in FLG (ranging from 5 to 17 layers) with the objective of understanding spin transport and spin relaxation mechanism in FLG.

The main focus is therefore to investigate how spin transport scales with the number of layers in FLG—finite stack of individual graphene layers bound together by van der Waals and π - π^* interactions. Inner layers of graphene can be thought of as being protected by the outer layers from any charge or spin scatterers sitting at the substrate or on top surface of FLG. These inner layers may ideally provide a cleaner path for spins transport along the layers due to screening of charges. Charge and spin transport measurements in FLG gives an idea on thickness dependence charge/spin diffusion coefficient D_c/D_s , spin life time τ_s and spin relaxation length λ_s .

1.3 Outline

In this thesis, I will present our measurements on spin injection, transport and detection in FLG based spintronic devices deposited on bare SiO₂ substrate.

To that end, the second chapter will be dedicated to a brief introduction to electronic and band properties of FLG followed by an explanation of the zone folding scheme utilized to calculate the diffusion coefficient within nearest

1. INTRODUCTION TO SPINTRONICS IN FEW LAYER GRAPHENE

neighbor tight binding calculations for our FLG samples. Moreover, basics of spin injection, transport and detection will be discussed.

In the third chapter, I will present detailed explanation of the making of FLG spin valve devices starting from mechanical exfoliation up until measurement techniques employed and the measurement setup used for studying spin transport measurements.

In the fourth chapter, I will present results from our spin transport measurements in FLG field effect transistors. Here result of charge transport measurements, non-local spin-valve and Hanle's spin precession measurements will be presented together with the extracted D_s , τ_s and λ_s for different number of layer of FLG.

The fifth and last chapter will be for discussion, conclusions and recommendations.

Chapter 2

Theory

A working spintronic device requires efficient spin injection, spin transport and detection. These processes are drastically affected by the choice of material and the nature of contacts. In our case we have FLG—single layers of graphene stacked on top of each other by weak van der Waals force. Since this thesis is dealing with spin transport in FLG, this chapter is organized in two sections. In the first section an introduction to electronic properties single layer graphene, bilayer graphene and finally of FLG is given. Starting from the electronic band structure of graphite, we obtain the electronic band structure of FLG by using the so called zone-folding scheme. To that end results of nearest neighbors tight binding calculations of bilayer graphene is used to understand the electronic structure of FLG in terms of effective coupling constants that vary with number of layers. Finally, the effect of screening of induced charges on the transport properties of lateral spin valve devices will wind up the section. In the second section, I will present basics of spin transport in a non-magnetic material in general and FLG in particular. The non-local geometry for spin transport measurements employed for our measurements is also presented along with issues related to spin injection, detection and transport.

2.1 Electronic properties of FLG

2.1.1 Single layer graphene, bilayer graphene and few layer graphene

Graphite consists of layers of single atomic thick carbon films, better known as graphene, stacked together. Graphene has carbon atoms arranged in an

2. THEORY

array of honeycomb structure. Figure 2.1a shows a typical graphene crystal structure. The lattice of graphene consists of two equivalent interpenetrating triangular carbon sublattices A and B containing one carbon atom each. Each atom has three nearest neighbors. Since there are 2 atoms per unit cell in graphene, it requires to solve a 2×2 Hamiltonian discussed elsewhere [25, 26, 27]. The lattice of graphene has two equivalent carbon atoms, designated

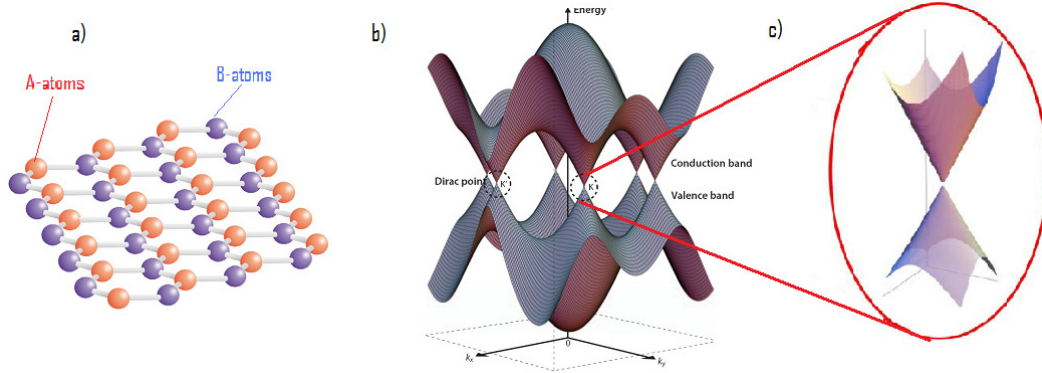


Figure 2.1: a) Graphene - one atomic thick array of carbon atoms arranged in hexagonal lattice. C-atoms shown in orange and blue represent C-atoms from the two sub-lattices. b) Electronic dispersion relation of graphene in the first Brillouin and c) Blow up at the k-point a.k.a. Dirac point showing a linear dispersion relation with no gap

A and B, per unit cell, and is invariant under 120° rotation. The resulting hexagonal lattice is therefore filled by sp^2 ($s - p_x - p_y$) hybridized C-atoms. The remaining p_z orbitals stick out of the plane forming bonding and anti-bonding-pairs with neighboring C-atoms. Since each C-atom contributes an electron for transport, in the ideal case graphene is metallic.

As shown in 2.1c, the conduction and valence bands cross each other at the K-points leaving graphene with no energy band gap. Hence, at low energy energies, the dispersion relation is linear:

$$E_F = \hbar v_F k \quad (2.1)$$

where v_F is the Fermi velocity. This linear dispersion relation leaves graphene with a vanishing density of states at the Fermi energy given by

$$\nu(E) = \frac{g_s g_v 2\pi}{\hbar^2 v_F^2} |E| \quad (2.2)$$

where $g_s = g_v = 2$ are the spin and valley degeneracy. However, due to disorder in the graphene and impurities the density of states at the Fermi energy is never zero but approaches to $2/\hbar v_F l$ [28], where l is the mean free path.

Graphene layers can be stacked in either of three ways: AA (simple hexagonal), AB (Bernal) or ABC (Orthorhombic) stacking types. Electronic band structures, anisotropy of transport properties, response to external field etc greatly varies with stacking order. For example, Bernal stacked trilayer graphene is a semimetal whereas orthorhombic trilayer is a semiconductor with parabolic dispersion relation [29, 30].

For the preparation of our graphite spin valve devices we use highly oriented pyrolytic graphite (HOPG) from GE Advanced Ceramics of grade ZYA which occurs naturally as an AB-stacking. In AB-stacking, C-atoms from sublattice A on the top layer are directly above each other and C-atoms from B-sublattice lies directly on top of the center of the hexagon of the lower layer. Fig 2.2 shows AB-stacked bilayer graphene with orbital overlap parameters γ_0 to γ_4 – which quantify the integral overlap of orbitals of C-atoms sitting at different lattice points on different layers (γ_1, γ_3 and γ_4) and in the same layer (γ_0).

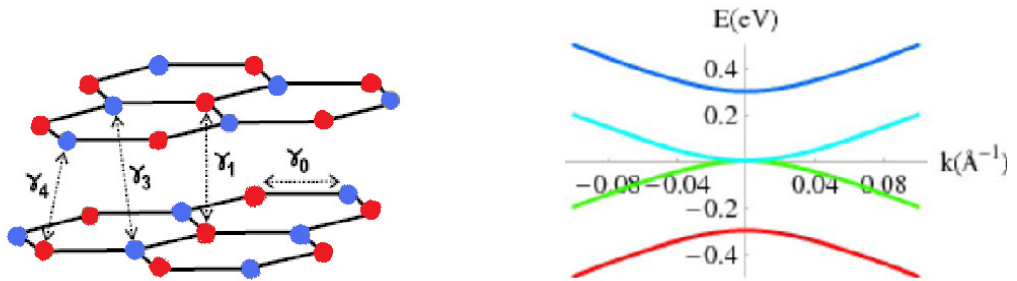


Figure 2.2: a) Crystal structure of a bilayer graphene with orbital overlap parameters γ_0 to γ_4 . b) Electronic dispersion relation of a bilayer graphene showing two parabolic subbands at the K-point.

Unlike in graphene, a bilayer graphene have a parabolic dispersion relation around the K-point. In a bilayer graphene a unit cell has 4 atoms—2 from each layer. Hence, the Hamiltonian one has to use will be of 4×4 dimensions. With in the nearest tight binding approximation, one can obtain an expression for the electronic dispersion relation near the K-point: [31]

$$E(k) = \pm\gamma_1 \pm \sqrt{\frac{\gamma_1^2}{4} + (\hbar v_f k)^2} \quad (2.3)$$

2. THEORY

where γ_1 is the interlayer coupling energy between two atoms of same sublattice (see 2.2) in different layers. Its value ranges from 0.3 to 0.39eV as determined by IR spectroscopy [32, 33] and Raman spectroscopy [34, 35].

The momentum for the lowest conduction sub-band in Eq. (2.3) will then be:

$$k = \frac{1}{\hbar v_f} \sqrt{E^2 + E\gamma_1} \quad (2.4)$$

Using this, one can calculate the density of states of a bilayer graphene at the K-point:

$$\nu(E) = \frac{g_s g_v}{2\pi \hbar^2 v_F^2} \left(E + \frac{\gamma_1}{2} \right) \quad (2.5)$$

Distinction between different number of layers of FLG requires systematic way of mapping the 3D graphite band structure to a 2D band structure. Depending on the number of layers (even or odd), the electronic band dispersion of FLG alternates from a linear to parabolic dispersion [29]. Therefore understand the evolution of the electronic band structure a systematic way of mapping the 3D band structure of graphite to finite stack of FLG is important. Figure 2.3

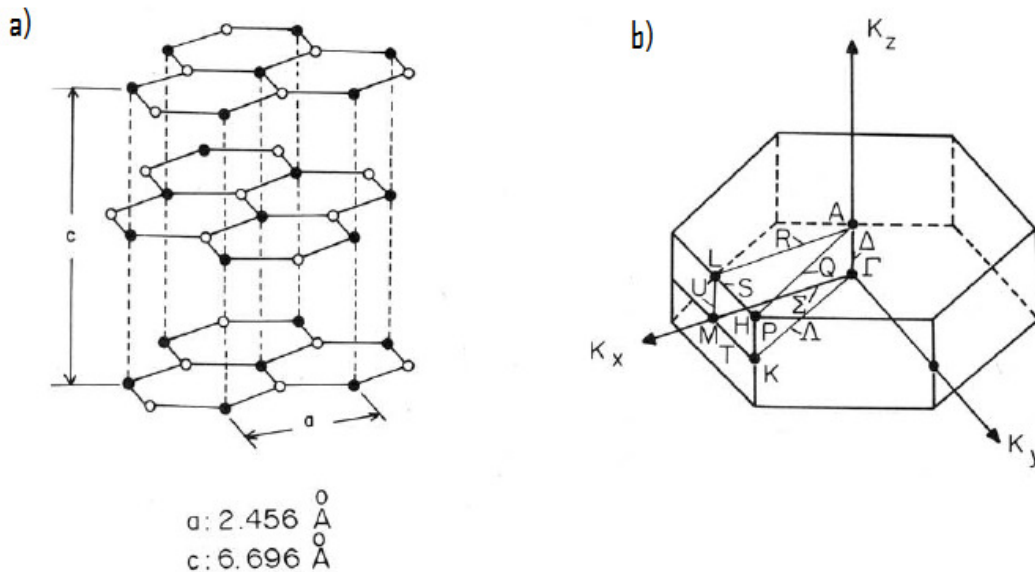


Figure 2.3: AB-stacked graphite (a) and its first Brillouin zone (b) from which the the 2D Brillouin zone is obtained by taking $k_z = 0$ plane.

shows a typical 3D-graphite crystal structure together with its first Brillouin zone obtained from nearest neighbor tight binding calculations pioneered by P. R. Wallace [25]. Recent theoretical work by Koshimo *et al.* [36] and IR absorption experiments by K.F. Mak *et al.* [37] showed that the Hamiltonian

of N-layer Bernal stacked system can be reduced to N/2 bilayer system for N even and N/2 bilayer plus one graphene layer for N odd. Hence starting from graphite band structure, it is possible to obtain the electronic band structure of FLG by using a simple model that reduces a 3D graphite to 2D FLG. This method is discussed in the next section.

2.1.2 Zone folding scheme

Zone folding is a relatively simple model which is a direct consequence of the periodicity of reciprocal lattice of the Brillouin Zones. It has been successfully used to calculate electronic band structure of carbon nanotubes by zone-folding of the π -bands of graphene [27, 38]. Using the zone folding model electronic band structure of FLG of any layer thickness N is obtained from the 3-D band structure of graphite by cutting at discrete values of k_z planes in the z-direction [37, 39, 40]. The number of cutting points through along k_z is determined by the number of layers. One important assumption in this approach is that for N-layers of graphene, the 0^{th} and $(N + 1)^{th}$ layers act as hard boundaries such that a standing wave is produced in the N-layer graphite perpendicular to the graphene planes. These cutting planes are given by:

$$k_z = \frac{2\pi n}{(N + 1)c} \quad (2.6)$$

where $c/2$ is the interlayer spacing of 0.34nm and the allowed value for the index $n = \pm 1, \pm 2, \pm 3, \dots \pm \frac{N+1}{2}$ (for odd N) and $\pm \frac{N}{2}$ (for even N). For any N-layer graphene system, the number of independent 2-D planes in the 3-D Brillouin zone (Fig. 2.3a), i.e., the number of new 2-D bands being created is given by the integer part of $\frac{N+1}{2}$. Using Eq. (2.6), $k_z = \{\frac{\pi}{c}\}$, $k_z = \{\frac{2\pi}{3c}\}$ and $k_z = \{\frac{\pi}{c}, \frac{\pi}{2c}\}$ can be obtained for single layer, bilayer and trilayer graphene respectively. This formalism thus reduces any N-layered graphite system of $2N \times 2N$ Hamiltonian to its equivalent 4×4 bilayer equivalent with a modified γ_1 as:

$$\gamma_{N,n} = 2\gamma_1 \cos\left(\frac{n\pi}{N + 1}\right) \quad (2.7)$$

For N even, each segment corresponds to the Hamiltonian of N/2 bilayers with an effective coupling. For N odd, we get $\frac{N-1}{2}$ effective bilayers and one single graphene. Hence the electronic band structure of FLG is reduced to the single layer and bilayer graphene band structures. Now using Eq. (2.4 - 2.7), we can

2. THEORY

write a more generalized density of states for FLG at $E = 0$ as:

$$\nu_N = \frac{\sum_n \gamma_{N,n}}{v_f^2 \pi \hbar^2} \quad (2.8)$$

Here the summation is done over the number of sub bands. For any N even, the number of sub bands is simply $\frac{N}{2}$ parabolic subbands and for odd N , an extra contribution from a single layer like sub band emerges. Figure 2.4a shows

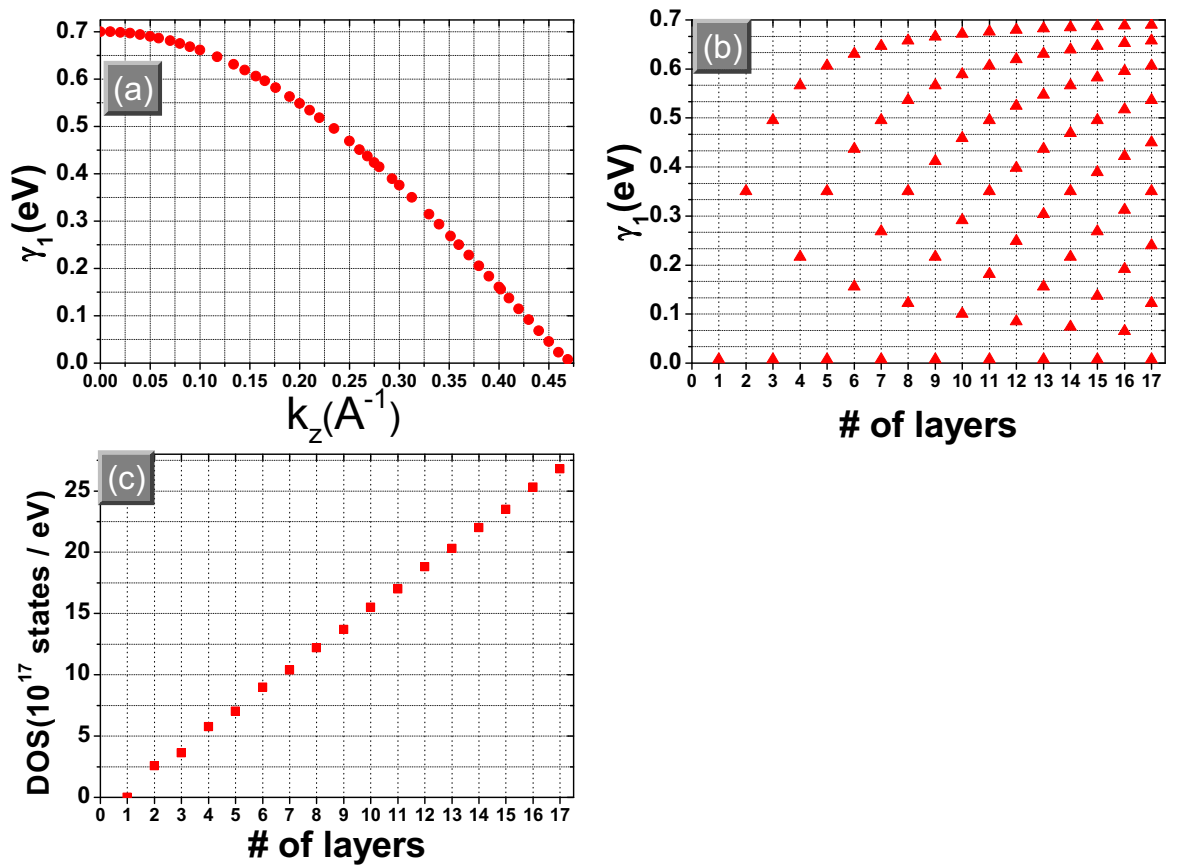


Figure 2.4: Effective coupling constant γ_1 as a function of a) cutting planes k_z , (b) of number of layers of graphene and (c) the resulting $\nu(E)$ for different number of layers.

the effective coupling constant γ_1 as a function of the cutting planes k_z . Now if we correlate the coupling constants and k_z with the number of layers we obtain the effective coupling constant as a function of the number of layers (Fig. 2.4b). As shown in Fig. 2.4c the obtained density of states shows a

linear increase with number of layers of FLG. We will use this density of states to calculate the charge diffusion coefficient D_c from Einstein's relation.

2.1.3 Screening in few layer graphene

One of the interesting aspects of spin transport in graphene is gate tunability of the spin signal. It has already been shown that it is indeed possible to influence spin transport by applying a gate voltage [9, 41]. Spin transport in FLG stacks can also be influenced by the gate voltage as we show in this thesis. This is reflected by the gate dependent spin precession measurements. However, complete understanding of influence of gate voltage on the spin transport requires understanding the effect of screening of induced charges. Theoretical [42] and experimental [43, 44] works have shown that the screening length in graphite is approximately 1nm (about 3-5 layers) which means the applied gate voltage is only felt weakly by layers sitting above 3 to 5 layers from the substrate. Consequently, most of the induced charges sit in those layers sitting closer to the gate. The charge distribution decays exponentially deep into layers in the bulk. A simple Thomas-Fermi model of screening of charges in FLG transistors is reported by Sui and Appenzeller [44]. In their model, an exponential decay of induced number of charge carriers from the gate is employed in a parallel resistor model of graphene layers with equal resistances. By taking the interlayer resistance into account they have also obtained screening length similar to previously reported values. We also follow similar model by assuming that only the top layer is makes contact to the current and voltage probes through which injection and detection of spins is done respectively. There are two consequences of the screening of charges. Firstly, since the gate voltage is felt only weakly by layers above the screening length, the contribution of these layers to the total conductivity is more or less constant which is broadly peaked over large range of the gate voltage. Secondly, as a result of screening of substrate induced impurity charges lying at the FLG/SiO₂ substrate, the life time of spins is expected to increase.

2.2 Spin transport in few layer graphene

A short introduction to spin transport in general and in non-local lateral spin valves in particular is presented. In this section, electrical means of spin injection and detection relevant to FLG are presented.

2.2.1 Electrical spin injection and accumulation

Spin injection into a non-magnetic material can be achieved by numerous ways. Optically, one can expose a sample, for example GaAs, to a circularly polarized light and hence the angular momentum of the photons will be transferred to the electrons making them spin polarized [45]. Another method is the electron spin resonance where first splitting of the degenerate spin up and spin down states is achieved by applying a magnetic field to the non magnetic (NM) material. Upon exposure to a microwave radiation an imbalance in spin densities can be created in the material due to spin excitations between Zeeman levels. Recently, spin Hall effect has also been used to show that spin accumulations can be achieved even without the application of a magnetic field where a reasonably high spin-orbit interaction plays the role of an external magnetic field sweeping the two spin species away to opposite sides of the sample [46, 47]. In this thesis, I will present the electrical means of injecting spins in to FLG systems of different thicknesses.

In 1976 Aronov proposed the possibility of injecting spins into NM materials by sending electrical current from a FM to a NM material (Fig. 2.5a) [48]. In a FM the density of states of majority and minority spin species are shifted in energy with respect to each other. Hence at the Fermi energy there is clear imbalance in populations of majority and minority spins. When a charge current is sent from the FM material through the FM/NM interface spin polarized current will be injected into the NM material. Due to sudden change in chemical potentials, spins accumulate at the interface. The resulting spin imbalance is referred to as spin accumulation (red arrows in Fig. 2.5a). Electric current in the NM can be explained by Mott's two channel model for conduction. This assumption holds also for our FLG spin valves where transport is diffusive. In this model, a current is assumed to be carried by two independent spin channels—one for spin up and one for spin down. Hence these two channels will have their specific chemical potentials (μ_{\uparrow} and μ_{\downarrow}) which drive current in these channels with different conductivities (σ_{\uparrow} and σ_{\downarrow}). The two spin components of electric current in the conductor can be written as:

$$j_{\uparrow} = \frac{\sigma_{\uparrow}}{e} \frac{\partial \mu_{\uparrow}}{\partial x} \quad \text{and} \quad j_{\downarrow} = \frac{\sigma_{\downarrow}}{e} \frac{\partial \mu_{\downarrow}}{\partial x} \quad (2.9)$$

The total electric charge current in the conductor is therefore:

$$j = j_{\uparrow} + j_{\downarrow} \quad (2.10)$$

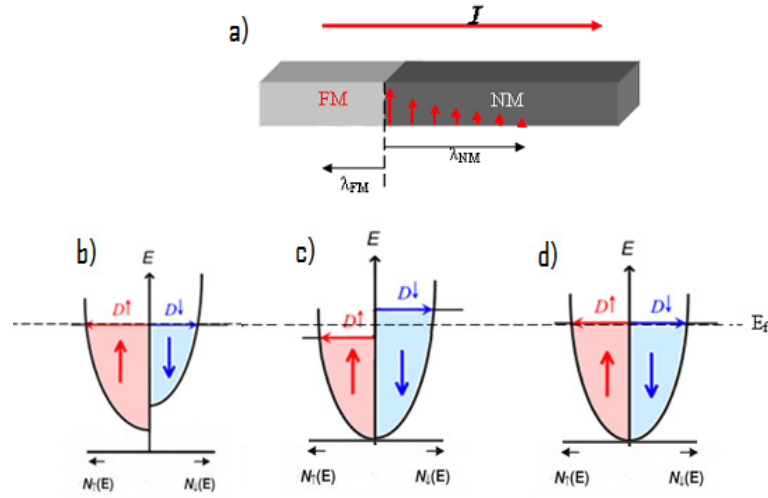


Figure 2.5: Electrical spin injection a) A current through a FM/NM interface creates spin accumulation at the FM/NM interface that decays exponentially away from the interface. b) density of states at the Fermi energy for a FM showing imbalance of spin species. c) resulting spin accumulation in a NM material with different chemical potentials for two spin species. d) shows density of zero spin polarization deep into the NM material where spin accumulation relaxed back to the equilibrium chemical potential far from the interface.

where as the spin current at the interface, which is the difference between current carried by individual channels, can be written as:

$$j_s = j_{\uparrow} - j_{\downarrow} \quad (2.11)$$

From the above two equations, the spin polarization of the electric current in the nonmagnetic conductor reads as:

$$P = \frac{j_s}{j} = \frac{j_{\uparrow} - j_{\downarrow}}{j_{\uparrow} + j_{\downarrow}} = \frac{\sigma_{\uparrow} - \sigma_{\downarrow}}{\sigma_{\uparrow} + \sigma_{\downarrow}} \quad (2.12)$$

The above equation assumes that spins are preserved during crossing the interface which is actually the case in spin injection experiments due to the additional tunnel barrier electrons must surpass before they enter to the NM region [11]. The tunnel barrier is used to combat the conductivity mismatch between the FM metal and NM few layer graphene (see sec. 2.2.3).

Spin accumulation in NM materials is a non-equilibrium phenomena. Hence spins accumulating near the interface need to relax back to the equilibrium state decaying exponentially as we go away from the interface. This process

2. THEORY

can be explained by a second order differential diffusion equation as:

$$D_s \frac{\partial^2 \mu_s}{\partial x^2} = \frac{\mu_s}{\tau_s} \quad (2.13)$$

where $\lambda_s = \sqrt{D_s \tau_s}$ is the spin relaxation length, D_s is the spin diffusion constant, τ_s is the spin relaxation time and $\mu_s = \mu_\uparrow - \mu_\downarrow$ is the chemical potential split between spin species during spin accumulation. A FM spin detector placed within the spin relaxation length probes spin accumulation as a chemical potential difference between the two spin channels and measures it as a spin signal voltage.

2.2.2 Detection of spin transport

A conventional two-terminal spin valve device can be used to extract spin transport related parameters. However it is difficult to distinguish spin transport from other effects that mimic the spin transport. It is generally a geometry which is prone to interference of other non-spin related effects, such as Hall effect and anisotropic magnetoresistance. A four-terminal non-local spin valve, on the other hand, (Fig. 2.6) avoids such spurious signals [8]. In such a geometry one needs to have four contacts of which at least two inner contacts are ferromagnetic. To facilitate device processing and do patterning of contacts in one lithography step, we make use of devices in which all contacts are FM. Different widths of FM contact ensure that each FM switches at different magnetic field value due to their shape anisotropy. By sweeping an in-plane magnetic field oriented parallel to the long axis of the contacts, it is possible to achieve the parallel or anti-parallel orientations between FM2 and FM3. In practice, outer FMs also act as injectors and detectors in which case 4-levels of resistance, instead of two, will be observed due to the contribution of outer FM1 and FM4 contacts [14].

When spins arrive at FM3, non-zero non-local voltage V_{NL} is measured by FM3 which changes sign with relative orientation of magnetization of FM2 and FM3. If FM2 is at $x=0$ and FM3 at $x=L$, the spin up chemical potentials in these regions are obtained by solving Eq. (2.13). For simplicity, let FM3 be within λ_s and let FM1 and FM4 be placed at a distance much larger than λ_s that chemical potentials of spin up and down equilibrates with the average chemical potential in FLG.

$$\mu_\uparrow = A \exp\left(\frac{x}{\lambda_s}\right) \quad \text{for } x < 0 \quad (2.14)$$

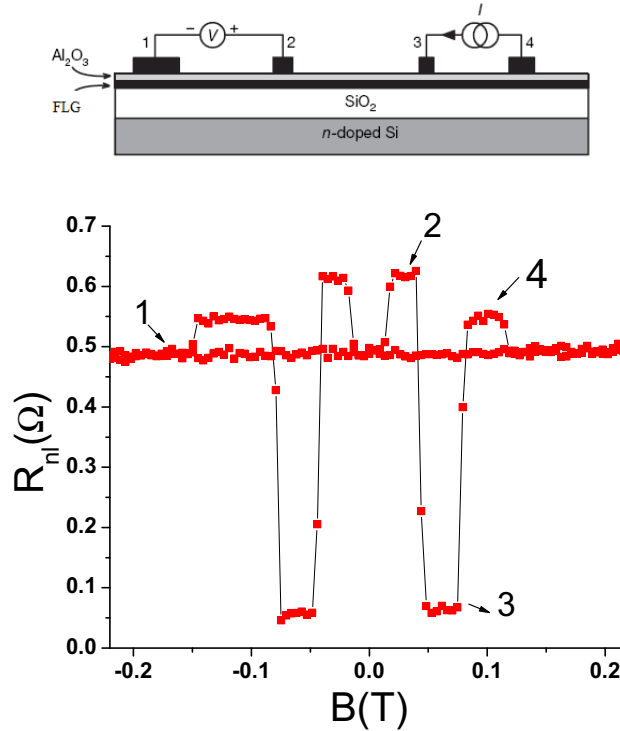


Figure 2.6: Detection of spin transport in a non-local geometry. Current only flows in the region between FM3 and FM4. FM2 detects diffusing spins from FM3. Depending on the relative orientation of FM2 and FM3 there exists two resistance levels (marked **1** and **3** for trace). Resistance levels marked by **2** and **4** are due to outer FM1 and FM4 that also act as injectors and detectors.

$$\mu_{\uparrow} = B \exp\left(-\frac{x}{\lambda_s}\right) + C \exp\left(\frac{x}{\lambda_s}\right) \quad \text{for } 0 < x < L \quad (2.15)$$

and

$$\mu_{\uparrow} = D \exp\left(-\frac{x}{\lambda_s}\right) \quad \text{for } x > L \quad (2.16)$$

For spin down species, the expressions for the chemical potential will be the same except that the coefficients A, B, C and D take either negative or positive depending on the orientation of the FMs. At equilibrium, the net chemical potential that FM3 detects translates to a non local of $\Delta V_{NL} = P\Delta\mu/2e$. For our FLG samples of length L , width W and conductivity σ , a non- local resistance ΔR_{NL} detected by FM3 is given by [14]:

$$\Delta R_{NL}(L) = \frac{\Delta V_{NL}}{I_{ac}} = \frac{P^2 \lambda_s R_{sq}}{W} \exp\left(\frac{-L}{\lambda_s}\right) \quad (2.17)$$

2.2.3 Conductivity mismatch and role of contacts

The signal obtained in Eq. (2.17) is strongly affected by the interface resistance. Normally, injection of spin polarized current into FLG requires a tunnel barrier. This is to combat the conductivity mismatch problem between the FM metal and the non magnetic low conductivity FLG since conductivity of FLG is by far smaller than that of Cobalt. The AlO_x barrier will play the role of matching the conductivities to assist injection of spins from low resistive Cobalt to high resistive FLG. The contacts should be transparent enough to allow spin injection but opaque enough to prevent spin relaxing back in to the ferromagnet. Popinciuc *et al.* incorporated the role contacts play as a spin relaxation route and obtained an expression for the non local resistance [14] given by:

$$\Delta R_{NL} = \frac{P^2 \lambda_s R_{sq}}{W} \frac{\left(\frac{R}{\lambda_s}\right)^2 \exp(-L/\lambda_s)}{\left(1 + \frac{2R}{\lambda_s}\right)^2 - \exp(-2L/\lambda_s)} \quad (2.18)$$

where R_c is the contact resistance and $R = (R_c/R_{sq})W$ is a spin relaxation factor that quantifies the role of contacts as a spin relaxation route. In the case when $R_c \rightarrow \infty$, Eq. (2.18) reduces to Eq. (2.17) in which case spins once injected do not relax back into the FM at the cost of losing energy to surpass the highly resistive contact. Rather they get transported along the FLG which is less resistive. For $R_c \rightarrow 0$, spins instead of going to the detector relaxes back in to the FM that, as a result, no spin signal is detected at FM2.

2.2.4 Spin relaxation in graphene and FLG

Different spin relaxation mechanisms: spin-orbit interaction (SO), hyperfine-interaction (HI), Elliot-Yafett (EY) spin relaxation mechanism, D'yakonov-Perel (DP) spin relaxation mechanism could contribute to spin relaxation in graphene based spin valve devices [13]. SO and HI are very small in case of carbon based materials because of the small atomic number and absence of nuclear spin respectively. The most dominant of all these mechanisms is found to be the EY mechanism where it was confirmed by linear scaling between momentum scattering time and spin relaxation time in graphene [41]. In this mechanism, spin relaxation occurs due to momentum scattering occurring due to impurities or defects. There is no lose in spin orientation in between scattering events. Hence the spin life time τ_s is directly related to the momentum scattering time. In other words, if any form of momentum scattering from impurities or defects are reduced, the spin life time of spins is expected to

increase. This is actually the main idea behind this thesis. Spin relaxation mechanisms in FLG could be similar to the case of graphene with some other extra contributions from interlayer hopping events that could potentially destroy spin polarization.

2.2.5 Hanle spin precession in FLG

When electrons are subject to a perpendicular magnetic field they undergo precession around the external magnetic field due to their intrinsic spin angular momentum. When a perpendicular magnetic field is applied to FLG, spins start to undergo a Larmor precession in the plane of the FLG flake at a frequency of $\omega_L = g\mu_B B/\hbar$. Now we can incorporate the effect of the perpendicular magnetic field into the diffusion equation (Eq. 2.13) as an extra term $\omega_L \times \mu_s$. Hence Eq. (2.13) reads as:

$$D_s \frac{\partial^2 \mu_s}{\partial x^2} - \frac{\mu_s}{\tau_s} + \omega_L \times \mu_s = 0 \quad (2.19)$$

If t is the time spins take to reach FM3 from FM2, spins acquire an additional angular rotation of $\phi = \omega_L t$. The detector electrode detects only the component of the spin parallel to its own magnetization direction. Hence the signal will be modulated by $\cos(\omega_L t)$ due to the applied field. In our FLG samples, since the device size is greater than any of the length scales, the phase acquired by individual spins is different due to a spread in diffusion time [49]. This is because there are many possible ways for spins to travel from FM1 to FM2. During this time possible spin flip can occur due to scattering from impurities. Hence by taking the probability of spin flip before reaching FM3 in to account, the non local resistance in Hanle precession measurement is given by:

$$R_{NL} \propto \int_0^\infty \frac{1}{\sqrt{4\pi Dt}} \exp\left(-\frac{L^2}{4Dt}\right) \exp\left(-\frac{t}{\tau_s}\right) \cos(\omega_L t) dt \quad (2.20)$$

Figure 2.7a shows schematic process of the spin precession experiment. A perpendicular magnetic field B_\perp applied to the NM material makes spins precess around it. In the parallel configuration, when injected spins arrive at the detector with their spin in the direction of the detector, then $\omega_L t = 0 \Rightarrow \cos(\omega_L t) = 1$ and hence R_{NL} is maximum shown by number 1 in Fig. 2.7b. When, on the other hand, spins arrive with their direction perpendicular to the detector, $\omega_L t = \pi/2 \Rightarrow \cos(\omega_L t) = 0$ and hence R_{NL} goes through 0 on the B -axis shown by number 2. If spins arrive at FM3 after acquiring an angular

2. THEORY

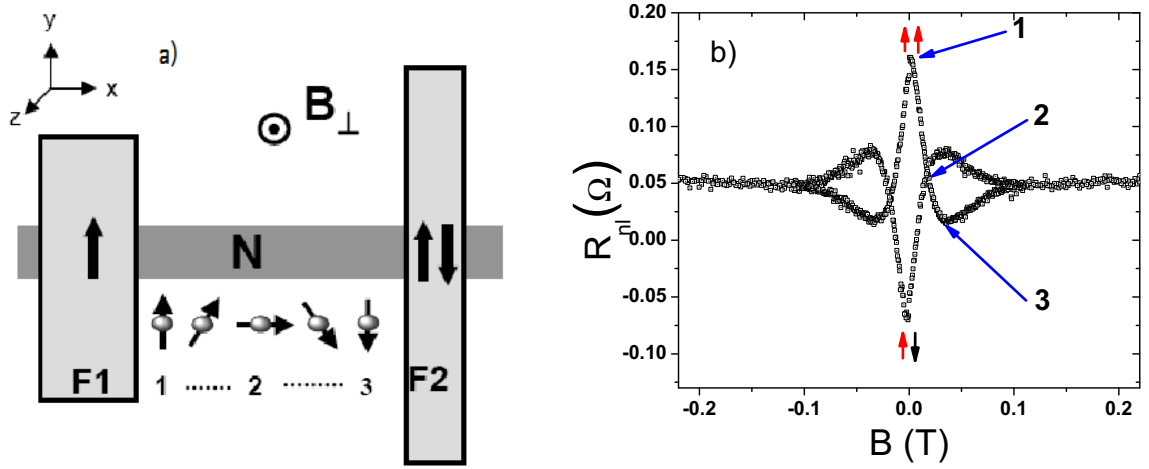


Figure 2.7: Spin precession in a perpendicular magnetic field. (a) shows the injector (F1) and detector (F2). If spins arrive at F2 with their orientation parallel to it, a maximum signal is obtained (number 1). If spins arrive perpendicular to F2 then a zero signal is measured (number 2). If spins arrive antiparallel to F2, a minimum signal number 3 is measured. (b) Three cases of precession numbered 1, 2 and 3 shown on a Hanle spin precession measurement.

rotation of π , the R_{NL} will take a minimum value which is shown by number 3 in Fig. 2.7 a and b. At relatively large magnetic fields the magnetization of the FM contacts is pulled up in the z-direction. This results in the increase of the R_{NL} resistance to the parallel signal obtained in a spin valve measurement. This is because at relatively high magnetic field, the magnetization of the FM contacts is pulled out of plane resulting in a parallel orientation of FM contacts. At this point the orientation of the magnetization of the contacts and the applied magnetic field is similar to a spin valve measurement except that the magnetization is in the z-direction. By fitting Fig. 2.7b with Eq. 2.20 we extract the spin diffusion coefficient D_s and the spin life time τ_s from which the spin relaxation λ_s is calculated.

Chapter 3

Experimental

Preparation of few layers graphene spin valve devices involve several steps. In this chapter we will first present details of the processes followed from deposition of FLG on SiO₂ substrate to characterization and measurement of the devices. In the second section, we will emphasize on our standard low frequency measurement techniques and the measurement setup that we use to characterize our spin valves. Processes mentioned in this chapter are followed for all spin valve devices studied through out the project.

3.1 Device preparation

3.1.1 Deposition of few layer graphene flakes

Deposition of graphene or FLG on SiO₂ is not as easy as the name of the process itself—mechanical exfoliation. It involves handful of steps of preparing a proper substrate before actually starting to mechanical exfoliate flakes off a highly oriented pyrolytic graphite (HOPG) and transfer them to SiO₂. A typical substrate is shown in Fig 3.1a. For highest contrast of graphene/FLG flakes a 300nm thick SiO₂ substrate is chosen. The SiO₂ has a predefined Au markers and Au contact pads that are defined by a photolithography step. They are used to map FLG flakes on the substrate as well as to find back FLG candidate flakes for further processing. Au contact pads are used to define a square where the FLG flake is located and to make contacts with the chip carrier during wire bonding. The deposition step is simply transferring FLG flakes from an HOPG graphite block of 1cm² to a SiO₂ substrate. This entire process is done in the clean room to avoid contamination. Commercially available HOPG graphite from GE Advanced Ceramics of grade ZYA is used

3. EXPERIMENTAL

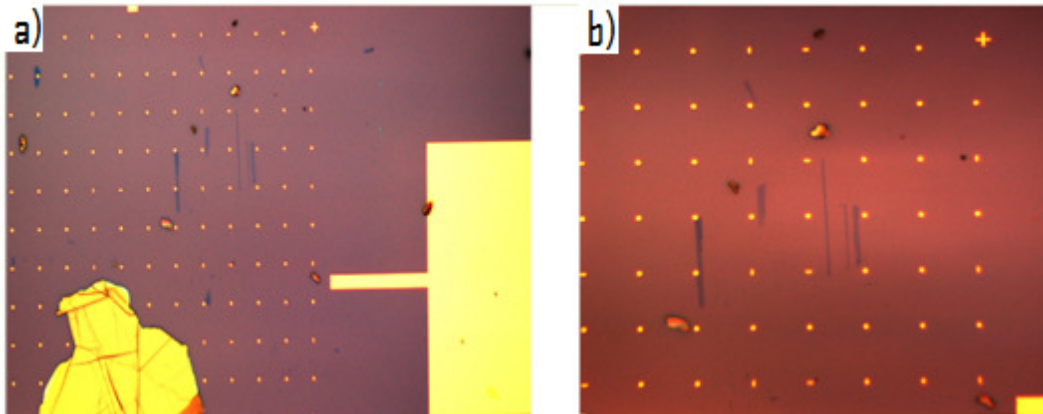


Figure 3.1: SiO₂ substrate used for deposition of FLG. a) shows FLG flakes deposited on the substrate by mechanical exfoliation. Small dots are Au markers spaced 14 μ m apart. The big rectangular pad is Au contact pad to which wire bonding will be made. b) Zoomed in picture: Bluish thin stripes are FLG flakes of approximately 14 μ m.

as a source from which flakes are exfoliated. We cleave layers of FLG from the HOPG block by putting a scotch tape on top. When the tape is lifted off the HOPG block it peels some FLG flakes with it. We now press the tape on the wafer by distributing equal pressure along the tape. In doing so, FLG flakes readily adheres to the substrate due to van der Waals forces. Finally the scotch tape is lifted slowly and the same procedure is repeated until a uniform flake distribution on the substrate is achieved. In this process care should however be given not to leave traces of unwanted source of contamination from the glue.

3.1.2 Selecting FLG flakes

After the deposition of FLG flakes we search for FLG flakes that are suitable for our spin valve devices. For this we use an OLYMPUS optical microscope to image FLG flakes in reflected light mode. Figure 3.1b shows an optical image of flakes of different thicknesses. For two main reasons, we tend to prefer flakes which are elongated and thinner to flakes which are wider. Firstly, one would like to put as many contacts as possible to be able to measure different regions of the flake in a non-local geometry. Secondly, the wider the flakes are the relatively smaller is the signal measured from the spin transport measurements.

When potential candidates are found, marker patterns previously defined on the substrate are used to map the position of the flakes and optical microscope images are used as aid to find back the FLG flakes for further processing of the sample.

3.1.3 Determination of number of layers

It is difficult to determine the number of layers of graphene a FLG candidate has using optical microscopy. We scan our FLG flakes by an atomic force microscopy (AFM). AFM is a high resolution surface scanning technique that can be used in different modes (Tapping, contact or non-contact). We use the tapping mode where the cantilever is made to oscillate at or slightly below its resonance frequency. On its lower point, the tip lightly taps the FLG sample surface during scanning. In tapping mode AFM, the cantilever is excited into

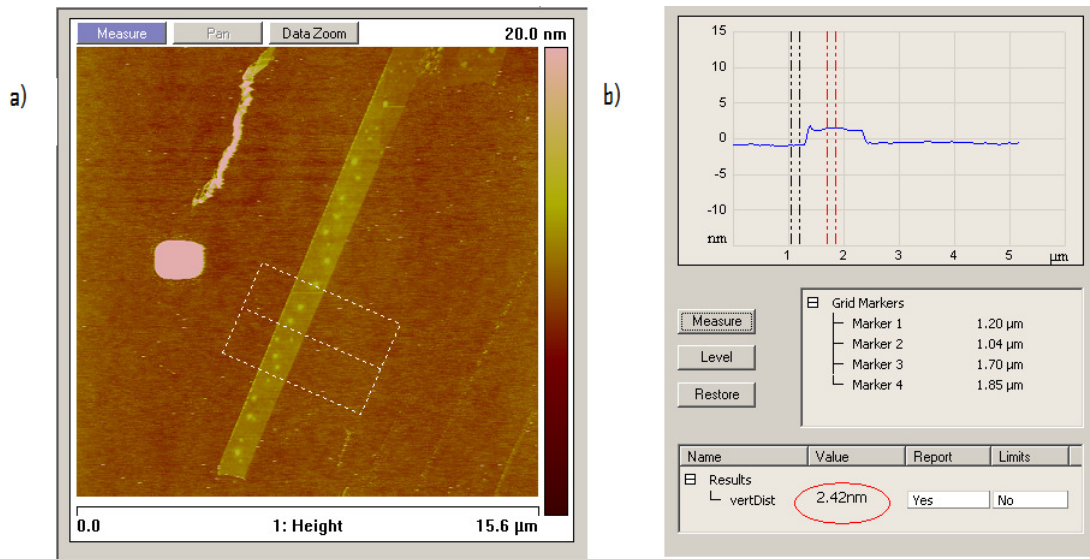


Figure 3.2: a) AFM height (topography) image of a FLG. To the right of the FLG flake. The rectangle shows the region from which the step height is measured. b) shows the step height measurement to determine the thickness of the flakes. The number circled with red is the measured height from which the number of layers of graphene is obtained by dividing this value with the interlayer spacing of 0.34nm.

resonance oscillation with a piezo driver. The oscillation amplitude is used as a feedback signal to measure topographic variations on the FLG surface. Depending on the topography of the FLG surface being scanned, the oscillation

3. EXPERIMENTAL

amplitude and the shift of resonance frequency changes. These changes are then interpreted as a height image by the help of the feedback circuit that tries to readjust the cantilever's oscillation amplitude. Figure 3.2 shows a height (topography) AFM image of 7 layers of FLG flake whose number of layers are determined by dividing the step height measured in Fig 3.2b by the interlayer spacing of 0.34nm. However, the number of layers of FLG determined this way are not conclusive since these values may be off by 1 layer. Hence we always do several step height measurements on different regions of the flake. Even then when we refer to our 7 layer of FLG as 7 ± 1 layers of graphene due to anomaly in thickness measurement. While determination of number of layers is one reason for AFM measurements, we also use the the AFM to check the homogeneity of the entire flake. Because sometimes a FLG flake may have cracks or folded regions. Once we know the number of layers, homogeneity and suitability of a FLG flake, we start to make a design for our device and deposit AlO_x barrier. These two steps are presented in the following two sections.

3.1.4 AlO_x deposition

An important component of our FLG spin valve devices is the tunnel barrier. As already mentioned in section 2.2.3, the conductivity mismatch problem is circumvented by putting an AlO_x barrier on top of FLG flakes. To that end, Aluminum deposition is done at UHV conditions at a rate of 1\AA per min for six minutes. Upon exposure to air the deposited Aluminum oxidizes and the total thickness of the AlO_x barrier will be 8\AA . To obtain a uniform coverage of the FLG flake by the Al, the sample holder is cooled to liquid nitrogen temperature to avoid migration/mobility of Aluminum on the surface of the flake. Apparently, the presence of pin-holes is inevitable [13].

3.1.5 Contact design and electron beam lithography (EBL)

Designing a FLG device necessitates consideration of the unique shape, length, orientation and neighborhood of the FLG flake of interest. This means we make individual designs for each FLG flakes. To be able to do a non-local spin and charge transport measurement, we need a minimum of four contacts. Normally, depending on the length of the flake we design our device such that there are more than 4 contacts on the device. This way we tend to have the choice for contact with reasonable contact resistances (see sec. 3.1.3). The

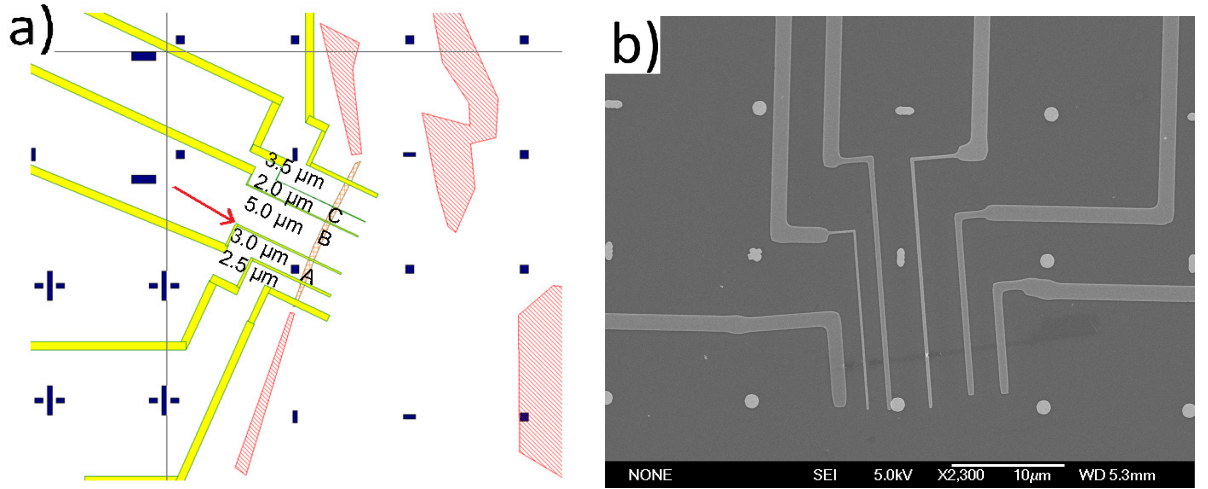


Figure 3.3: a) shows a schematic design of a FLG flake contacted by six contacts. The 90° turns (shown in red) insure that domains are broken and uniform switching of the ferromagnets is achieved while sweeping magnetic field. b) shows scanning electron microscope image of a FLG device. Device dimensions can be shown from the scales in the SEM picture.

contact widths, which determine the switching (coercive) field, range from 90nm to 500nm. The center to center distance between contacts in the region where spin transport is examined is normally 2 - $5\mu\text{m}$ long. Design is done in e-LINE program - same program used during EBL process. This program allows design of different components of the devices structures in different layers. For accurate positioning of our FLG flakes into the design program we use a Glass2k program that helps to make a window transparent such that it is possible to draw the shape of FLG flake in to the design program from another image window. Figure 3.3a shows a typical design of a FLG spin valve. It shows six ferromagnetic contacts of variable widths which are also shown along with the distances between the contacts. We design small contacts to spread out from the FLG flake by using $1\mu\text{m}$ wide lines. In the process, we have to avoid dirt particles or any other flakes around to avoid breakage or shorting of contacts¹. For the big contacts though going over a dirt particle is not risky since we use 10 or $12\mu\text{m}$ wide lines. An important aspect in contact design is to get a uniform switching of the ferromagnetic contacts. This is achieved by making a 90° turn on the ferromagnetic contacts, shown by red

¹In one case, it was not be possible to get away from going over a FLG flake. But it was possible to avoid shorting of contacts by crosslinking a PMMA polymer on top of the FLG flake and letting the contacts go over this insulating solid polymer.

3. EXPERIMENTAL

arrows in Fig. 3.3. These turns insure that domains are broken and uniform switching of the ferromagnets is achieved while sweeping magnetic field. We then finish up these lines with a small square pads so as to allow overlap with the big contacts that run from these pads to the predefined Au contact pads. This is because, during EBL step, the exposure of the small contacts and the big contacts is done at a different steps of the exposure and if in case during this time there is a pronounced drift in the beam, the risk of broken contacts is taken care of by these small square pads. Having the deposition of AlO_x done and the design of contacts completed, we pattern our design on the polymer using an EBL. For this we use a Raith EBL system with which contacts as small as 90nm can be written in our particular devices. The resolution of the contacts written is determined by the thickness of the polymer, the acceleration voltage and the type of the polymer used. For our case we use a polymer called polymethylmethacrylate (PMMA) as an e-beam resist. Since a high resolution is obtained with 950k PMMA of 2% solution, we spun this polymer at 4000RPM so as to obtain 70nm thick polymer layer on top of our FLG flakes. We then bake the polymer at 170°C for 90sec on a hot plate to evaporate the solvent from the polymer. Exposure of the PMMA layer to an accelerated

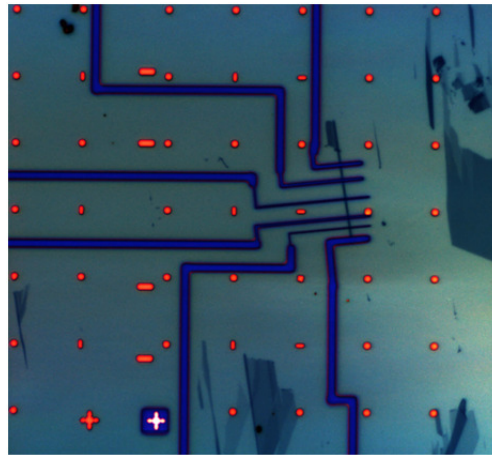


Figure 3.4: A sample after the development step. When a sample is dipped in a 1:3 ratio mixture of IPA:MIBK, the exposed part of the PMMA which has broken C–C chains is dissolved leaving the design patterned on the PMMA. The white cross (down left) is Au cross marker used during EBL step. The the FLG (dark blue) covered by PMMA is visible under an optical microscope.

beam of electrons leaves the covalent bonds of the polymer broken at places where the beam hits the polymer. The total amount of charges arriving at the

surface of the polymer is $100\mu\text{Ccm}^{-2}$. We can, however, vary this value by changing the dose factor. We use a dose factor of 1.5 and 2.0 for small and big contacts respectively. Dose factors are optimized for different width of FM contacts by taking in to account the effect of proximity and thickness of PMMA used. Since we only allow the beam to hit the polymer by activating only the layer we want to expose, the PMMA will have now the design structure of this specific layer patterned on it. After exposure, we dip the sample in to a 1:3 mixture of MIBK (MethylIsoButylKetone) and IPA (IsoPropylAlcohol) developer. As a result, the exposed area of the PMMA will be dissolved. The sample is softly moved around in this mixture to facilitate the development for about 70 seconds. For further cleaning we put the sample in IPA for 30 seconds and blow it dry with nitrogen. Now we check the developed sample under an optical microscope to see if we have actually achieved the desired structures shown in Fig. 3.3. A sample after the developments step is shown in Figure 3.4.

3.1.6 Ferromagnetic metal electrode deposition

After the development step we will deposit our ferromagnetic metal electrodes. This is done in an e-gun evaporation system (Temescal TFC2000) at a base pressure of 10^{-7} mbar. We normally deposit 30-35nm of Co at a rate of $1\text{\AA}/\text{sec}$ on top of the developed sample with zero angle evaporation. This ensures that the Co is not deposited on the walls of the developed section of the PMMA. The whole surface of the sample is now covered by a continuous film of Co except at the edges of the 70nm deep structures from the development step. If we can by any means dissolve the PMMA away, all the Co films on the polymer will be lifted off along with the polymer leaving only the Co that adhered to the SiO_2 . This is the process commonly known as the Lift-off process and the result of this process is shown in Fig. 3.5.

3.1.7 Lift-off and wire bonding

The final step in the fabrication process is lift off. Within this step, the remaining resist is dissolved by immersing the sample in hot acetone (around 40°) for 10 minutes. In doing so, the acetone dissolves the PMMA on the sample lifting with it off anything which is on the polymer off. Before proceeding with the wire bonding step, we examine the sample under an optical microscope to

3. EXPERIMENTAL

check if the Lift-off process worked out well. If there still exists unwanted Co

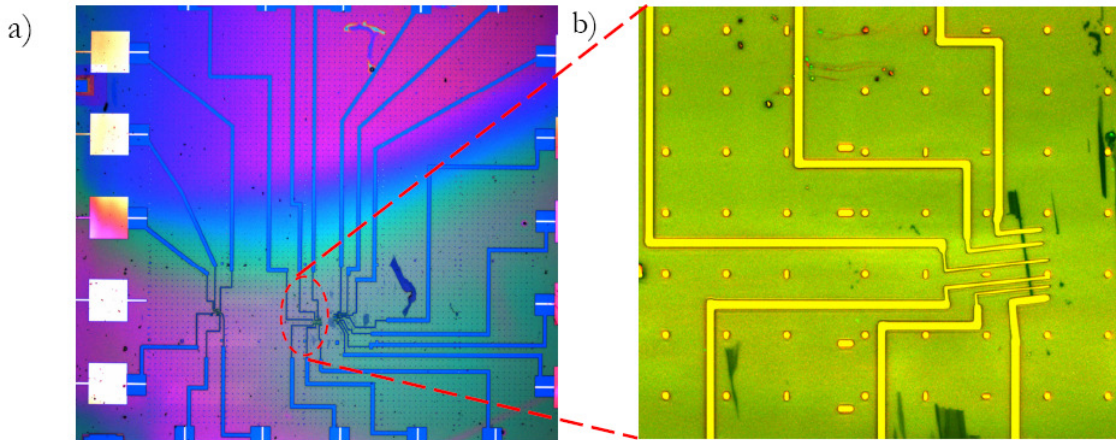


Figure 3.5: A sample after the lift-off process where the structures designed before in Fig. 3.3 are obtained. a) shows an overview picture ($5\times$ magnified) of the sample taken after the lift off step. Three FLG samples are also visible. The FLG sample is contacted to the square Au contacts pads (predefined on the substrate) b) shows zoomed-in ($100\times$ magnified) picture of the middle FLG (green stripe) sample which is contacted by six Cobalt (yellow) contacts.

structures that possibly short contacts, the lift-off process is repeated again until the required structures appear. Figure 3.5 shows the sample after the lift-off process. It shows the EBL patterned structures contacting the FLG flake that run to contact pads (see Fig. 3.5b). Following the lift off process is the wire bonding. The sample is now carefully glued to a chip carrier using a silver paste. We use a 16 or a 24 pin chip carriers. Wire bonding is done by using ultrasonic wire bonding. Square Au contact pads shown in Fig. 3.5b are used to contact the sample to the chip. This process should be done as quick as possible to avoid extreme oxidation of Co contacts. During the wire bonding process care has to also be given to not blow up a sample due to an electrostatic discharge. To that end a bonder has to ground himself.

3.2 Measurement setup

Once wire bonding is completed the sample is attached to a sample holder and transferred to a turbo pump to avoid further oxidation of the Co electrodes. Since the spin signals we measure are the order of 1Ω or less, we perform all measurements with a very sensitive way of detecting these signals. Spin

transport measurements are done in a standard low-frequency lock in technique in vacuum and at room temperature. A schematic picture of the measurement setup is shown in Fig. 3.6 with a description in the caption. An AC current which is controlled by a Lock-in amplifier (Stanford Research System SR830)

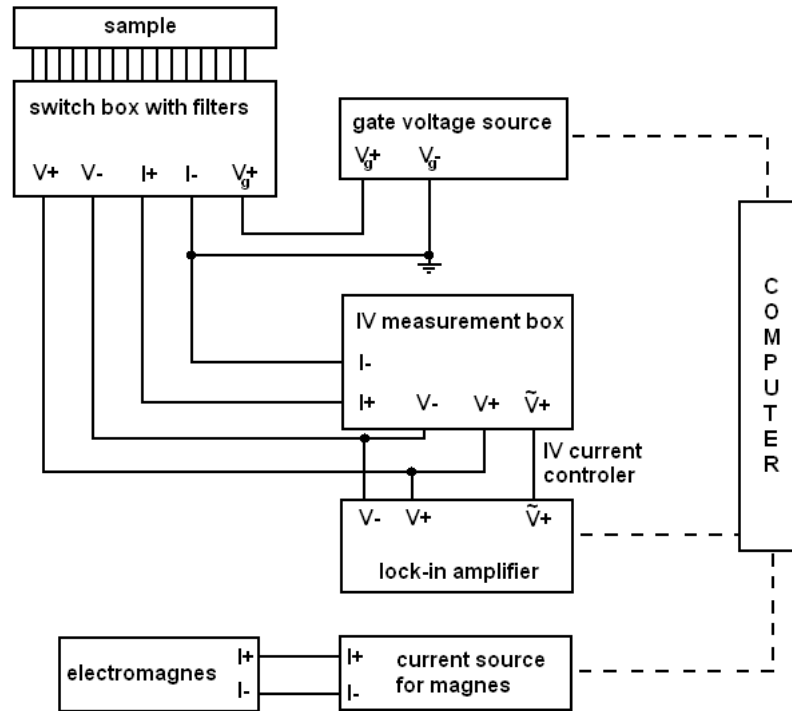


Figure 3.6: A schematic non local 4-probe measurement setup. A Lock-in instrument is connected to IV measurement box. It sends an ac voltage to the IV measurement box which translates it to an AC current. This AC current is sent to the sample. The voltage drop measured by $V+$ and $V-$ is then sent back to the IV measurement box which is amplified and sent back to the lock-in amplifier. The lock-in measures both the in-phase and out-of phase parts of the signal using a phase-locked loop technique.

is sent to the sample from the IV measurement box with a specific frequency of around 17Hz. This AC current is phase-locked with a reference signal from the lock-in amplifier. The resulting AC voltage measured from the sample is sent back to the IV measurement box which is amplified and again sent to the lock in amplifier. The lock in, therefore, measures both the in phase and out of phase component of the output signal by comparing it with the reference signal. In our charge transport measurement typical phase differences between the output and the reference signal are in the order of 1-8°. In our non-

3. EXPERIMENTAL

local spin transport measurements we get a phase in the range of 85-95° due to some capacitive couplings. For the safety of the sample, the sample box, which essentially acts as a switch, is equipped with π -filters of 1k Ω and 1nF each. They filter out any unwanted high voltage or high frequency peaks from the environment or any other sources which can potentially make the samples short-lived.

Normally we characterize our FLG spin valve devices with charge and spin measurements. In the charge transport measurements, we first start out by measuring multiprobe (2-, 3- and 4- probe) local resistances of the FLG flake. These measurements are very important to understand the quality of our sample, the level of dopants, the nature of the contacts etc.... One special property of graphene based FETs is the possibility to easily induce charge carriers by sweeping the back gate voltage (supplied by a Keithley 6517A). From this measurement the dependence of square resistance R_{sq} as a function of V_g is obtained. R_{sq} (also referred to as resistivity) is used in calculating charge diffusion coefficients. Therefore, all spin valve devices studied in this thesis are characterized with such type of measurements before any spin transport measurements are done.

In the spin transport measurements, first we check if a spin valve signal exists in a specific region of the FLG flake. To that end we sweep the magnetic field in the region of -0.6 to 0.6T using an electromagnet (GMW, model 5403). Second we perform Hanle spin precession measurement on the same region. For this we rotate our sample such that the magnetic field is perpendicular to the sample. From this measurement we extract the spin diffusion coefficient and the spin life time by fitting the measurement with Eq: (2.20). By Measuring the Hanle spin precession while sweeping the gate voltage, we obtain gate dependent D_s and τ_s from a routine fit procedure.

Chapter 4

Measurements

In this chapter, charge and spin transport measurements performed on FLG spin valve devices are presented. Details of the charge transport measurement are presented in the first section and the second section is dedicated to spin transport measurements. In the last section we compare results from both measurements specially comparison of spin and charge diffusion coefficients will be made.

4.1 Charge transport measurements

Room temperature charge transport measurements are used to calculate the charge diffusion coefficient D_c which we finally compare with the spin diffusion coefficient extracted from a room temperature spin transport measurements. We perform 4-probe resistance measurement of the FLG samples. In a 4-probe measurement (Fig. 4.1a) we measure the voltage using the inner contacts while sending electrical current between the outer contacts. This way we only measure the resistance of the FLG while excluding the resistance of the contacts since no current flows through the contacts to the voltage probe [50]. The measured resistance is normalized by the ratio of the length of the measured FLG area to its width W to obtain the sheet (square) resistance R_{sq} - commonly referred as resistivity (in ohms) [15, 51]. By applying a gate voltage, V_g a charge density of $n = \epsilon_o \epsilon (V_g - V_{Dirac}) / te = \alpha (V_g - V_{Dirac})$ is capacitively induced in the FLG, where ϵ_o and ϵ are the permittivities of free space and SiO_2 respectively; e is the electron charge; t is the thickness of SiO_2 layer (300nm) and the constant $\alpha = 7.2 \times 10^7 \text{cm}^{-2} \text{V}^{-1}$.

4. MEASUREMENTS

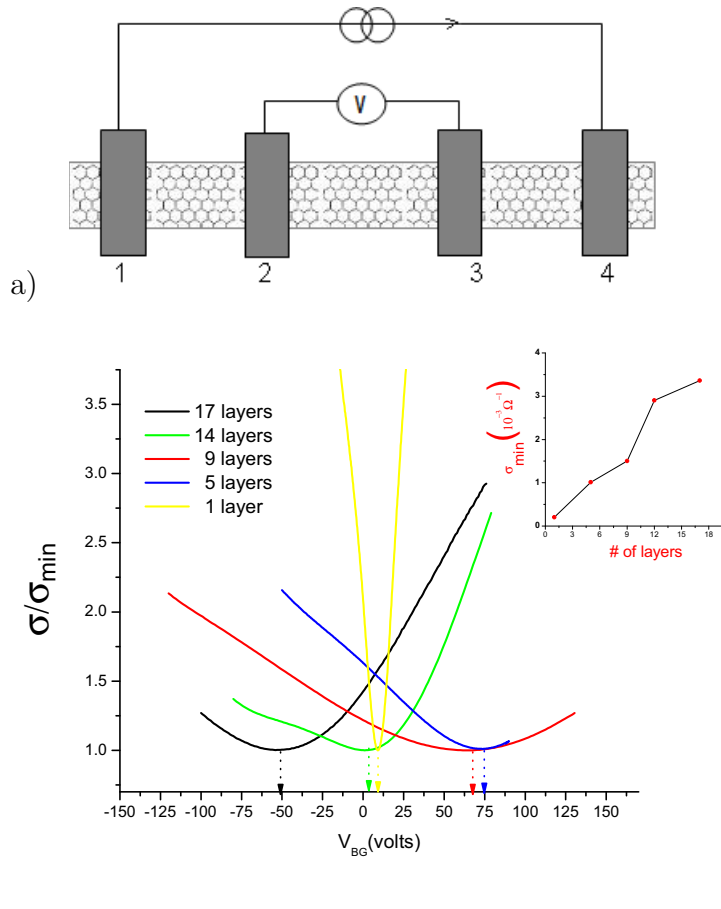


Figure 4.1: a) 4- probe geometry for measuring resistance of FLG b) Conductivity of FLG of 1, 5, 9, 14 and 17 layers normalized to the minimum conductivity σ_{min} for each sample. The inset shows the linear scaling of the peak resistance with the number of layers. Two samples were heavily p-doped, one was n-doped and one was not doped which can be seen from the shift of the conductivity minima.

Fig. 4.1b shows the conductivity $\sigma=1/R_{sq}$ (in $1/k\Omega$) as a function of the applied gate voltage for samples with varying thicknesses ranging from 1 to 17 layers. The curves are normalized by the minimum values at the Dirac point σ_{min} . The conductivity takes a broad minimum at the Dirac point (a.k.a. Dirac Point) where there exists mixed charge carriers of electrons and holes. The inset shows the linear scaling of the conductivity minimum σ_{min} at the Dirac point as a function of the number of layers N . The broadening of the conductivity curve increases with the number of layers (as compared to graphene [15]) owing to contribution from inner layers to the total conductivity. This is because the induced charge carriers decay with $\exp(\frac{-x}{\lambda})$ as a result

of screening: where x is the distance from the substrate and $\lambda = 1 - 2\text{nm}$ corresponding to 3 to 5 layers. Conductivity of layers sitting above 3 to 5 layers from the substrate can be modulated by the gate voltage only weakly which results in overall broadening of the curve. From the charge transport measurement and calculated DOS obtained in chapter 2 (see Eq. 2.8), we can calculate the charge diffusion coefficient D_c at the Dirac point ($\epsilon_F=0$) with the Einstein's relation $D_c = 1/R_{sq}e^2\nu(\epsilon_F)$ where D_c is the charge diffusion coefficient, $\nu(\epsilon_F)$ is the density of states at the Dirac point. To obtain the

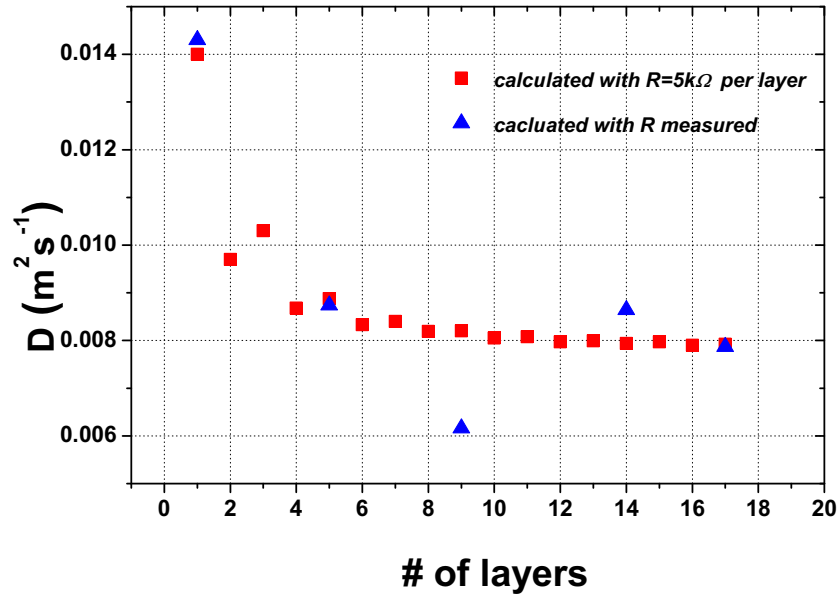


Figure 4.2: Calculated charge diffusion coefficient by using Einstein's relation at the Dirac point for different numbers of layers. For this calculation, the measured conductivity along with the calculated DOS at the Dirac point are used.

density of states for FLG, the zone-folding scheme was used with in the nearest neighbor tight binding approximation method. With this simple method the variation of the density of states with the number of layers was calculated (see sec. 2.1.2). Then this result is used to calculate the charge diffusion coefficient at the Dirac point. Fig. 4.2 shows the dependence of the calculated charge diffusion coefficient with number of layers. It is not clear yet why the charge diffusion coefficient decreases with number of layers.

4.2 Spin transport measurements

To fully characterize spin transport in our FLG spin valve devices we perform two standard spin transport measurements—spin valve measurement and Hanle spin precession measurements—in a non local geometry. The first measurement is to check if a spin signal exists in the region of interest and the second type of measurement is used to extract D_s and τ_s from which λ_s is calculated.

4.2.1 Spin valve measurement

We perform spin valve measurements in a non local geometry where contributions from unwanted background magnetoresistances, such as the anisotropic magnetoresistance and the Hall effect are excluded [4, 8]. The geometry is

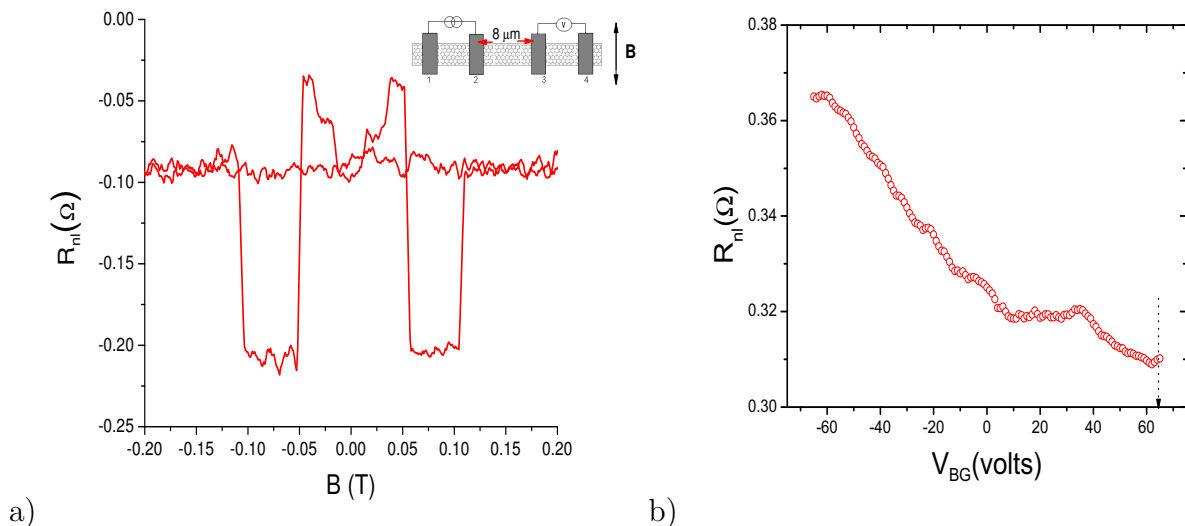


Figure 4.3: a) Spin valve measurement over $8 \mu\text{m}$ length with zero back gate voltage. In the inset is shown the non local geometry. The small signal observed in this measurement is because of the length of the active region over which the measurement was done. b) shows the dependence of the spin signal with gate voltage.

shown in the inset of Fig. 4.3a where a result of such measurement is shown. We first apply an external magnetic field to align all FM contacts in parallel orientation. We send current from FM1 to FM2 and measure the non local resistance R_{nl} with FM3 and FM4 as explained in chapter two. If we now measure the non-local voltage with the detector, a constant non-zero background

$R_{nl} (\approx -0.1\Omega)$ is measured probably due to capacitive effects and other related phenomena like intershell conductance [52].

By sweeping the magnetic field, we achieve the antiparallel orientation when one of the inner electrodes (say the detector) switches. This results in a relatively higher R_{nl} ($\approx -0.21\Omega$). Further increase of the external magnetic field switches all FMs again back to the parallel orientation. A typical spin valve measurement at zero gate voltage is shown in Fig. 4.3 along with the non local geometry employed for the measurement. As opposed to two levels in the non-local resistance that should be observed, there are four clearly visible resistance levels. The origin of these levels is due to the contributions from the outer contacts which themselves act as a detector and injector [9, 14]. The relatively small signal ($\approx 0.1\Omega$) is due to the large distance between the spin detector and injector which in this case was $8\mu\text{m}$ —the largest distance ever over which spin transport in graphene based spin valve devices is measured.

Dependence of spin signal on the gate voltage can be measured by performing a spin valve measurement for different gate voltage. From this the dependence of the spin signal over the induced charge carriers is obtained. To measure the gate dependent spin signal we first achieve a parallel orientation of electrodes and measure the signal at zero magnetic field while sweeping the gate voltage. A similar measurement is repeated for an antiparallel orientation. The difference between the parallel and antiparallel signals $\Delta R_{nl} = |R_{nl,P} - R_{nl,AP}|$ obtained from such measurement is plotted against V_g and is shown in Fig. 4.3b. The spin signal shows a broad minimum at the Dirac point where the conductivity, density of states, diffusion coefficient and number of induced charge carriers are also minimum (see Fig. 4.1). The origin of the decaying spin signal towards the Dirac point is yet to be understood completely but can be explained intuitively from the expressions obtained for R_{nl} in Eq. (2.17 and 2.18). The non-local resistance R_{nl} is directly proportional to both the resistivity R_{sq} of FLG and the spin relaxation length λ_s . The square resistance $R_{sq} = \sigma^{-1}$ is maximum at the Dirac point. However the spin signal does not increase towards the Dirac point like R_{sq} which would mean that λ_s should take a minimum around the Dirac point. For large number of induced charge carriers the signal increases monotonically as we go far into the two metallic regime extremes. This observation is also supported by our Hanle spin precession measurements which we discuss next.

4. MEASUREMENTS

4.2.2 Hanle spin precession measurement

The second part of the spin transport measurements is the Hanle spin precession measurement. Upon application of an out-of-plane magnetic field to the FLG flake, spins start to precess around the magnetic field in the plane of the FLG. This effect is not only an unequivocal means to confirm presence of spin transport in FLG but also a means used to extract the spin diffusion coefficient D_s and spin life time τ_s . Hanle spin precession measurement was successfully

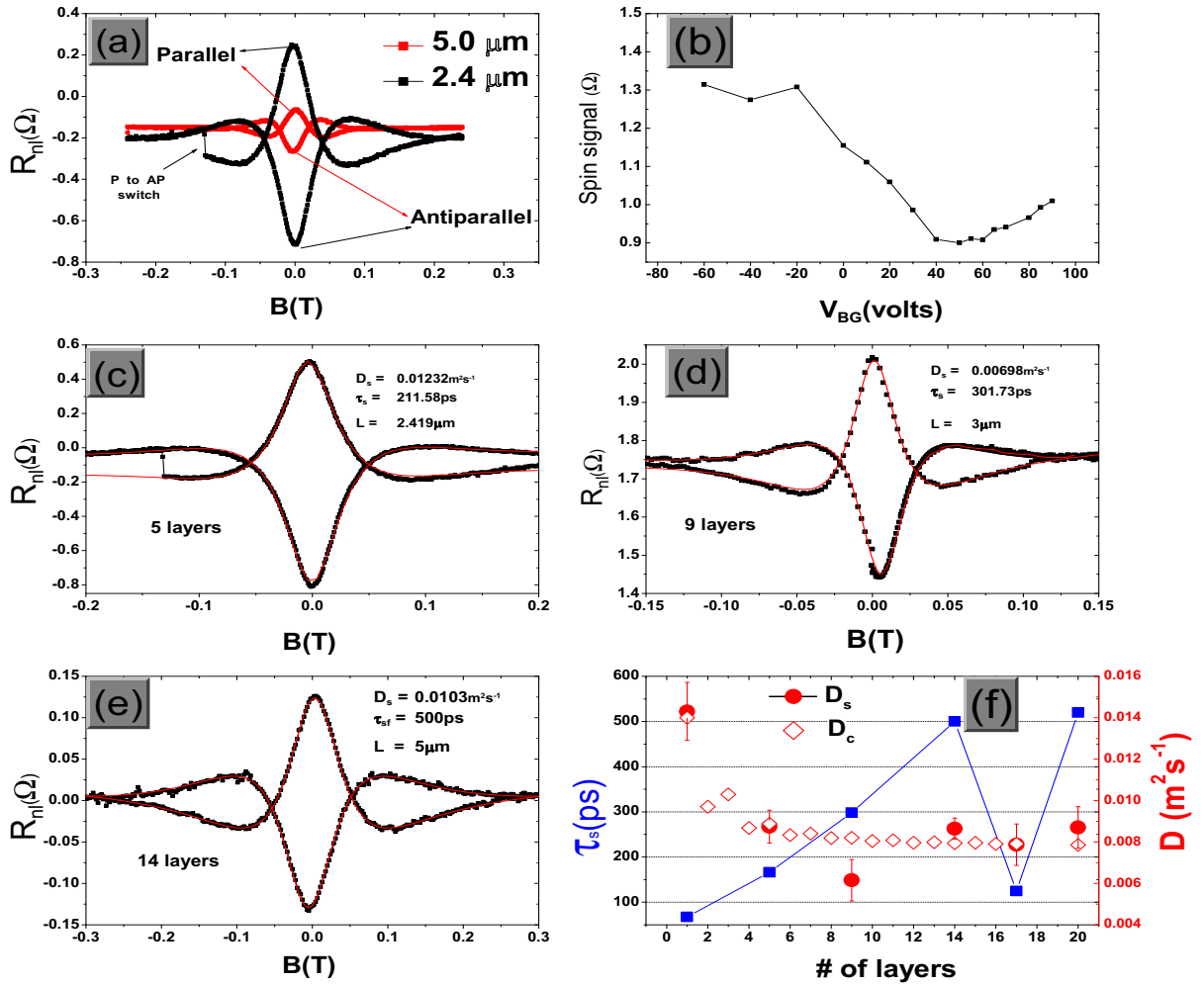


Figure 4.4: Spin precession in FLG. a) Spin precession for $V_g=80\text{V}$ for $2.4\mu\text{m}$ and $5\mu\text{m}$ long region of FLG of 5 layers. b) Spin signal obtained from series of precession measurements at different gate voltages showing the trend in Fig. 4.3. c), d) and e) show fits of Hanle spin precession measurements for 5, 9 and 14 layers together with the extracted D_s , τ_s and the distance L over which precession is measured. f) shows dependence of τ_s , D_c and D_s with number of layers. The point for the single layer graphene was taken from ref. [41]

performed on FLG devices of 5, 9, 14 and 17 layers of 1-5 μm long. The basic principles of the Hanle spin precession measurement is presented in sec. 2.2.5. To perform this measurement we should first switch the inner contacts to parallel or antiparallel orientation before we apply an out-of-plane magnetic field. To switch between P and AP orientations with ease, for example in a gate dependent spin precession measurement, it is important that we have an in-plane magnetic field component that can switch the FMs at high magnetic fields. This is achieved by applying an external magnetic field which is by few degrees off the ideal out-of-plane direction. At relatively higher magnetic field, the in-plane component allows for relative control of the injector/detector magnetization orientation. The advantage of the in-plane component is visible in Fig. 4.4a where switching from AP to P orientation is obtained without physically rotating the magnet. Figure 4.4a shows the result of a spin precession measurement done over 2.4 μm and 5 μm long region of 5 layers of FLG flake at $V_g=80\text{V}$. At $B=0$, the signal is maximum/minimum for the parallel/antiparallel orientation. The difference between the signals for parallel and antiparallel at $B=0$ is equal to the spin signal obtained from a spin valve measurement. As is visible from the graph, the peak-to-peak signal is higher for $L=2.5\mu\text{m}$ than for $L=5\mu\text{m}$ as expected from the dependence of the spin signal on length. Upon applying an out-of-plane magnetic field spins start to precess and the spin signal is modulated by the field (see Fig. 2.7 in section 2.2.5). Fig. 4.4b shows peak-to-peak spin signal obtained by subtracting the R_{AP} from R_P at $B=0\text{T}$ for different gate voltages (induced charge carriers). The spin signal obtained this way agrees well with the one obtained from the gate dependent spin valve measurement.

By fitting spin precession curves with Eq: (2.20) we extract the spin transport parameters— D_s and τ_s . Fits of the precession measurement for three samples of 5, 9 and 14 layers of FLG are shown in Fig. 4.4 along with the extracted parameters from the fit. As shown in Fig. 4.4(f), the spin life time increases monotonically with the number of layers and starts to saturate for thicker systems. It is known that the most dominant spin relaxation mechanism in graphene based spin valves is the Elliot-Yaffet mechanism. Spin relaxation through spin-orbit and hyperfine interactions are negligible. The monotonic increase in spin life time with the number of layers naturally suggests that somehow intrinsic spin flip scattering mechanisms are reduced in FLG spin valves due to the screening of substrate induced momentum scattering potential. Finally, comparison of charge and spin diffusion coefficient is

4. MEASUREMENTS

made. The density of states calculated from a nearest neighbor tight binding approximation presented in Fig. 2.4 along with the measured square resistance $R_{sq} = 1/\sigma$ is used to calculate D_c for various number of layers of FLG devices. Fig. 4.4f shows the calculated charge diffusion coefficient plotted against the number of layers. The calculation was done for two R_{sq} values—one by taking $5k\Omega$ per layer which is usually observed in our FLG devices and another by taking the measured R_{sq} (see Fig. 4.2). The spin diffusion coefficient extracted from the Hanle spin precession measurement is also plotted in the same graph. The calculated charge diffusion coefficients are with in the same order as those obtained from the Hanle precession measurement. Given the simplicity of the model we used, we can argue that the charge and spin diffusion coefficients are similar at the Dirac point in agreement with the previous work [41].

4.2.3 Gate dependent spin precession measurement

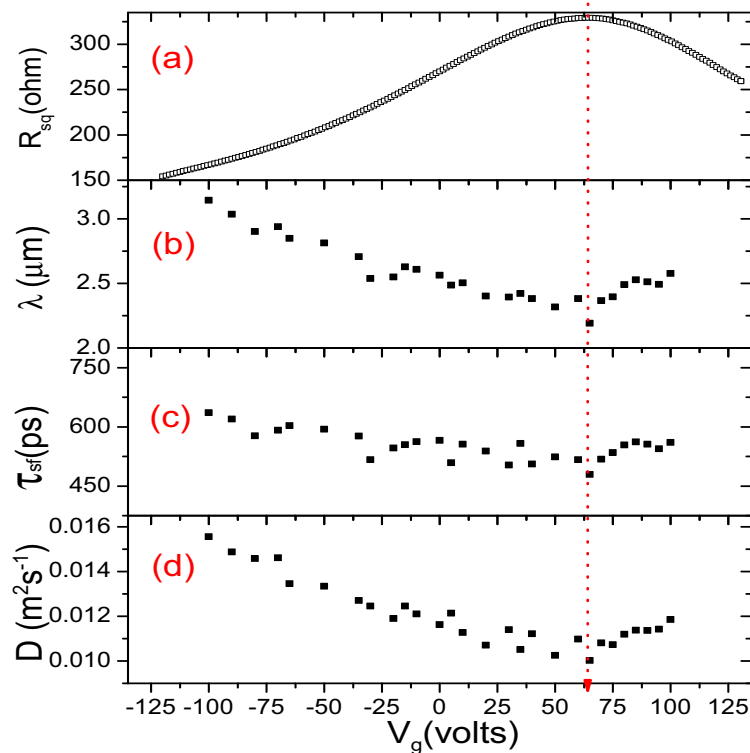


Figure 4.5: Gate dependent spin transport in FLG. a) shows the square resistance of 14 layers of FLG used to calculate the charge diffusion coefficient, b) shows the spin relaxation length $\lambda_s = \sqrt{D_s \tau_s}$ calculated from the spin life time τ_s in (c) and the spin diffusion coefficient D_s in (d).

To understand how spin precession in FLG is affected by the number of induced charge carriers, we performed gate dependent spin precession measurements from which gate (induced number of charge carriers) dependence of D_s and τ_s are extracted. To that end, several Hanle precession measurements are done at various gate voltages. We extract the gate dependent D_s and τ_s by fitting all precession curves. Fig. 4.5 is result of such measurements showing the dependence of D_s and τ_s with the induced number of charge carriers/gate voltage. In Fig. 4.5a the square resistance R_{sq} is shown. The maximum of the curve is situated at $V_g \approx 65V$ (the so called Dirac point) due to unintentional hole doping of the FLG flake. Both D_s and τ_s decrease and approach a minimum of $0.01\text{m}^2\text{s}^{-1}$ and 100ps respectively at the Dirac point (shown by red dotted line). Away from this point both values increase to $0.015\text{m}^2\text{s}^{-1}$ and 500ps respectively. Since $\lambda = \sqrt{D_s\tau_s}$, it also follows the same kind of behavior as the spin diffusion coefficient and life time. From panels (b) and (d) of Fig.

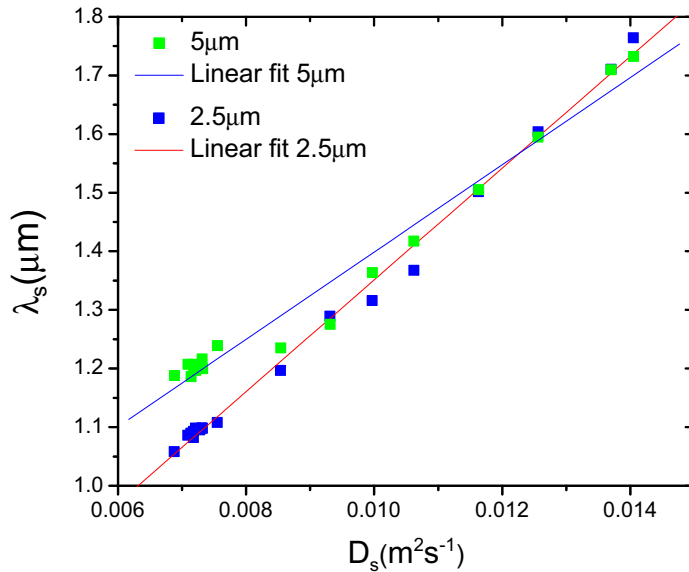


Figure 4.6: Linear relationship between λ_s and D_s for 5 layers of FLG. Green dots are for $5\mu\text{m}$ long region of the FLG flake where as blue square dots are for $2.5\mu\text{m}$ long region. Linear fits are also shown.

4.5 we see that there exists a linear dependence between the spin relaxation length and the diffusion coefficient as opposed to the relation $\lambda_s = \sqrt{D_s\tau_s}$. This result confirms that the main spin relaxation mechanism is the Elliot-Yaffet spin relaxation mechanism as is evident from Fig.4.6 which is plotted

4. MEASUREMENTS

for two different regions of 5 layers FLG. This is in agreement with earlier reports for graphene spin valve devices [14, 41]. This result also supports the observed increase of spin life time with increasing number of layers of FLG. Since most of momentum scattering in graphene based field effect transistors is induced by the substrate [53, 54, 55], the screening of these charged scattering potentials in FLG explains why τ_s increases with number of layers.

Chapter 5

Conclusions

We studied spin transport in FLG devices with various number of layers ranging from 5 to 17. All devices were prepared following similar procedures (see appendix). The 4-probe charge transport measurements show that the minimum conductivity at the Dirac point increases monotonically with increasing number of layers—the minimum being for single layer. Another observation is the broadening of the so called Dirac curve with increasing number of layers i.e. the Dirac curve for a single layer graphene is sharply peaked around the Dirac point whereas that of FLG is broader. This is the result of the effect of screening of charges by induced charge carriers on layers closer to the substrate. In other words, most of the induced charge carriers sit in the lower 3-5 layers. The effect of the electrostatic potential from the gate is weakly felt by upper lying layers. Hence the total conductivity will be broadly peaked around the Dirac point.

With in the nearest neighbor tight binding approximation of bilayer graphene, a unified zone folding scheme was applied to graphite to calculate the density of states at the Dirac point. The calculated density of states is used to calculate the charge diffusion coefficient from Einstein's relation. Given the simplicity of our model, the charge diffusion coefficient obtained from this calculation is in good agreement with that obtained from spin transport measurements.

We also showed that spins in FLG relax by way of the Elliot-Yafet mechanism. Plots of λ_s as a function D_s show that there exist a linear relationship between them as opposed to the expected $\lambda_s \propto D_s^{1/2}$ (from the definition of the spin relaxation length). This is a clear confirmation for the dominance of the Elliot-Yafet spin relaxation mechanism in few layer graphene systems. Moreover, the longer spin life times in FLG systems, which are a factor of 3 or 4 times higher than in graphene, also support the dominance of the Elliot-Yafet

5. CONCLUSIONS

mechanism. This is because impurity induced momentum scattering potentials from the substrate are screened as thickness of the samples increase. Reduction of momentum scattering from these impurities makes spins in FLG long lived. It is not yet completely clear what kind of other contributions exist towards spin relaxation apart from the Elliot-Yafet spin relaxation mechanism. For instance, the interlayer diffusion could introduce spin relaxation since the time scale that the interlayer diffusion occurs is not yet known. This requires further investigation to understand whether spins are preserved during interlayer spin diffusion or not.

Finally, from our spin transport measurements, we have shown that D_s at the Dirac point is by a factor of 3 smaller than that in graphene. The decrease in spin diffusion coefficient with number of layers could be due to probable interlayer hopping between layers of graphene.

Appendix A

Device fabrication recipe for FLG spintronic devices

In this appendix, we summarize the device fabrication procedures followed in the preparation of our FLG samples.

A.1 FLG deposition

1. Take a heavily doped Si (n^{++}) wafer with 300nm SiO_2 which has previously defined Au/Cr markers on it (see ref.[48] for recipe on how to prepare the substrate and the Au/Cr markers).
2. Cut the wafer in to required size. Clean the substrate afterwards by blowing to get rid off glass pieces.
3. Use a scotch tape to cleave a thin 1 by 1 cm^2 graphite layer of an HOPG block.
4. Press the scotch tape on the substrate and push firmly on the wafer by distributing equal pressure along the tape.
5. Lift the scotch tape and repeat step 4 to another region on the wafer.

A.2 FLG flake selection & characterization

6. Select few layer graphene candidates by using optical microscopy in reflected light mode. Use Au markers to map candidate flakes on the substrate for further processing of the device.
7. Determine the thickness of the flakes using tapping mode AFM. Also check for homogeneity of flake by looking for cracks or folds in the flake.

A.3 Tunnel barrier deposition and EBL

8. Deposit 6Å thick Aluminum layer on the sample in UHV and at liquid nitrogen temperature. Then oxidize it to produce an 8Å thick Al₂O₃ layer.
9. Spin coat PMMA 950k (2% in ethyl lactate-n-Butyl acetate) at 4000rpm for 1 minute so as to obtain 70nm PMMA layer. Anneal the wafer on a hot plate for 90sec at 170°C.
10. Use EBL (10kV), dose 100μC/cm², dose factor 1.5, to expose the small field with a 10μm aperture. Use a 1.8 dose factor to make 150nm wide contacts (design 130nm), use a 2.6 dose factor to make a 90nm wide contacts (design 50nm).
11. Repeat step 10 to expose the big field with a 60μm aperture. Use a 1.8 dose factor to make 150nm wide contacts (design 130nm), use a 2.6 dose factor to make a 90nm wide contacts (design 50nm).
12. Develop in a 1:3 mixture of MIBK:IPA (Methyl Iso Butyl Ketone 99.5%:Iso-Propyl Alcohol) for 70sec, rinse in IPA for 30sec and blow dry using nitrogen gas. Check contact structures by optical microscope if the development step worked out well.
13. Deposit 30-35nm thick cobalt using e-gun evaporation system (Temescal TFC2000) at a rate of 1Å/sec at a base pressure of 10⁻⁷mbar.
14. Do lift off in warm acetone at a temperature of about 40°C for 10 minutes, rinse in IPA for 30sec and blow dry using nitrogen gas. Check

sample using optical microscope if desired sample structure is achieved. Otherwise, repeat until required structure is obtained.

15. Wire bonding: glue sample to a chip carrier using a silver paste. The sample now is connected to the gate on the chip carrier through the silver paste. Connect sample and the chip carrier using ultrasonic wire bonding. Write down the pin numbers for each contact. Do not keep the sample too long in open air since the contact properties (resistance, spin injection efficiency etc...) change as Co oxidizes. Hence proceed to the next step as quickly as possible.
16. Put the sample in to vacuum to avoid oxidation of cobalt. Connect sample to the setup and measurements can be started.

A. DEVICE FABRICATION RECIPE FOR FLG SPINTRONIC DEVICES

References

- [1] Baibich, M. N. *et al.* Giant magnetoresistance of (001)Fe/(001)Cr magnetic superlattices. *Phys. Rev. Lett.* **61**, 2472–2475 (1988). [1](#)
- [2] Binasch, G., Grünberg, P., Saurenbach, F. & Zinn, W. Enhanced magnetoresistance in layered magnetic structures with antiferromagnetic interlayer exchange. *Phys. Rev. B* **39**, 4828–4830 (1989). [1](#)
- [3] Datta, S. & Das, B. Electronic analog of the electro-optic modulator. *App. Phys. Lett.* **56**, 665–667 (1990). [1](#)
- [4] Jedema, F., Filip, A. & van Wees, B. Electrical spin injection and accumulation at room temperature in an all-metal mesoscopic spin valve. *Nature* **410**, 345–348 (2001). [2](#), [32](#)
- [5] Jedema, F. J., Heersche, H. B., Filip, A. T., Baselmans, J. J. A. & van Wees, B. J. Electrical Detection of Spin Precession in a Metallic Mesoscopic Spin Valve. *Nature* **416**, 713–716 (2002). [2](#)
- [6] Lou, X. *et al.* Electrical detection of spin transport in lateral ferromagnet-semiconductor devices. *Nature Physics* **3**, 197–202 (2007). [2](#)
- [7] Takahashi, S. & Maekawa, S. Spin Injection and Detection in Magnetic Nanostructures. *Phys. Rev. B* **67**, 052409 (2003). [2](#)
- [8] Tombros, N., Jozsa, C., Popinciuc, M., Jonkman, H. T. & van Wees, B. J. Electronic Spin Transport and Spin Precession in Single Graphene Layers at Room Temperature. *Nature* **448**, 571–574 (2007). [2](#), [14](#), [32](#)
- [9] Cho, S., Chen, Y.-F. & Fuhrer, M. S. Gate-Tunable Graphene Spin Valve. *App. Phys. Lett.* **91**, 123105 (2007). [2](#), [11](#), [33](#)

REFERENCES

- [10] Hill, E., Geim, A., Novoselov, K., Schedin, F. & Blake, P. Graphene Spin Valve Devices **42(10)**, 2694 – 2696 (2006). [2](#)
- [11] van Wees, B. Semiconductor spintronics: Spins go their own way. *Nat Phys* **3**, 147–148 (2007). [2](#), [13](#)
- [12] Rashba, E. I. Theory of Electrical Spin Injection: Tunnel Contacts as a Solution of the Conductivity Mismatch Problem. *Phys. Rev. B* **62**, R16267–R16270 (2000). [2](#)
- [13] Tombros, N. *Electron spin transport in graphene and carbon nanotubes*. Ph.D. thesis, Zernike Institute of Advanced Materials (2008). [2](#), [16](#), [22](#)
- [14] Popinciuc, M. *et al.* Electronic spin transport in graphene field-effect transistors. *Physical Review B* **80** (2009). [2](#), [3](#), [14](#), [15](#), [16](#), [33](#), [38](#)
- [15] Bolotin, K. *et al.* Ultrahigh Electron Mobility in Suspended Graphene. *Solid State Communications* **146**, 351 – 355 (2008). [2](#), [29](#), [30](#)
- [16] Geim, A. K. Graphene: Status and Prospects. *Science* **324**, 1530–1534 (2009). [2](#)
- [17] Huertas-Hernando, D., Guinea, F. & Brataas, A. Spin-orbit coupling in curved graphene, fullerenes, nanotubes, and nanotube caps. *Phys. Rev. B* **74**, 155426 (2006). [2](#)
- [18] Huertas-Hernando, D., Guinea, F. & Brataas, A. Spin-orbit-mediated spin relaxation in graphene. *Phys. Rev. Lett.* **103**, 146801 (2009). [2](#)
- [19] Józsa, C., Popinciuc, M., Tombros, N., Jonkman, H. T. & van Wees, B. J. Electronic Spin Drift in Graphene Field-Effect Transistors. *Physical Review Letters* **100**, 236603 (2008). [2](#)
- [20] Józsa, C., Popinciuc, M., Tombros, N., Jonkman, H. T. & van Wees, B. J. Controlling the Efficiency of Spin Injection into Graphene by Carrier Drift. *Physical Review B* **79**, 081402 (2009). [2](#)
- [21] Józsa, C., Popinciuc, M., Tombros, N., Jonkman, H. & van Wees, B. Electronic spin drift in graphene field-effect transistors. *Physical Review Letters* **100** (2008). [2](#), [3](#)

-
- [22] Stauber, T., Peres, N. M. R. & Castro Neto, A. H. Conductivity of suspended and non-suspended graphene at finite gate voltage. *Phys. Rev. B* **78**, 085418 (2008). [3](#)
- [23] Adam, S. & Sarma, S. D. Transport in suspended graphene. *Solid State Communications* **146**, 356 – 360 (2008). [3](#)
- [24] Meyer, J. C. *et al.* The structure of suspended graphene sheets. *Nature* **446**, 60–63 (2007). [3](#)
- [25] Wallace, P. R. The band theory of graphite. *Phys. Rev.* **71**, 622–634 (1947). [6](#), [8](#)
- [26] Geim, A. K. & Novoselov, K. S. The Rise of Graphene. *Nature Materials* **6**, 183–191 (2007). [6](#)
- [27] Saito, R., Dresselhaus, G. & Dresselhaus, M. S. *Physical Properties of Carbon Nanotubes* (World Scientific Publishing Company, 1998). [6](#), [9](#)
- [28] Peres, N. M. R., Guinea, F. & Neto, A. H. C. Electronic properties of disordered two-dimensional carbon. *Physical Review B* **73**, 125411 (2006). [7](#)
- [29] Castro Neto, A. H., Guinea, F., Peres, N. M. R., Novoselov, K. S. & Geim, A. K. The electronic properties of graphene. *Rev. Mod. Phys.* **81**, 109–162 (2009). [7](#), [8](#)
- [30] Lu, C. L., Chang, C. P., Huang, Y. C., Chen, R. B. & Lin, M. L. Influence of an electric field on the optical properties of few-layer graphene with ab stacking. *Phys. Rev. B* **73**, 144427 (2006). [7](#)
- [31] McCann, E. & Fal’ko, V. I. Landau-level degeneracy and quantum hall effect in a graphite bilayer. *Phys. Rev. Lett.* **96**, 086805 (2006). [7](#)
- [32] Kuzmenko, A. B., Crassee, I., van der Marel, D., Blake, P. & Novoselov, K. S. Determination of the gate-tunable band gap and tight-binding parameters in bilayer graphene using infrared spectroscopy. *Phys. Rev. B* **80**, 165406 (2009). [8](#)
- [33] Zhang, Y. *et al.* Direct observation of a widely tunable bandgap in bilayer graphene. *Nature* **459**, 820–823 (2009). [8](#)

REFERENCES

- [34] Malard, L. M. *et al.* Probing the electronic structure of bilayer graphene by raman scattering. *Phys. Rev. B* **76**, 201401 (2007). [8](#)
- [35] Gava, P., Lazzeri, M., Saitta, A. M. & Mauri, F. Probing the electrostatic environment of bilayer graphene using raman spectra. *Phys. Rev. B* **80**, 155422 (2009). [8](#)
- [36] Koshino, M. & Ando, T. Orbital diamagnetism in multilayer graphenes: Systematic study with the effective mass approximation. *Phys. Rev. B* **76**, 085425 (2007). [8](#)
- [37] Mak, K. F., Sfeir, M. Y., Misewich, J. A. & Heinz, T. F. The Electronic Structure of Few-Layer Graphene: Probing the Evolution from a 2-Dimensional to a 3-Dimensional Material. *ArXiv e-prints* (2009). [0908.0154](#). [8](#), [9](#)
- [38] Popov, V. N. & Henrard, L. Comparative study of the optical properties of single-walled carbon nanotubes within orthogonal and nonorthogonal tight-binding models. *Phys. Rev. B* **70**, 115407 (2004). [9](#)
- [39] Reich, S., Maultzsch, J., Thomsen, C. & Ordejón, P. Tight-binding description of graphene. *Phys. Rev. B* **66**, 035412 (2002). [9](#)
- [40] Dubois, S. M.-M., Zanolli, Z., Declerck, X. & Charlier, J.-C. Electronic properties and quantum transport in graphene-based nanostructures. *The European Physical Journal B* **72**, 1–24 (2009). [9](#)
- [41] Józsa, C. *et al.* Linear scaling between momentum and spin scattering in graphene. *Phys. Rev. B* **80**, 241403 (2009). [11](#), [16](#), [34](#), [36](#), [38](#)
- [42] Guinea, F. Charge distribution and screening in layered graphene systems. *Physical Review B* **75**, 235433 (2007). [11](#)
- [43] Miyazaki, H. *et al.* Inter-Layer Screening Length to Electric Field in Thin Graphite Film. *Applied Physics Express* **1**, 034007 (2008). [11](#)
- [44] Sui, Y. & Appenzeller, J. Screening and Interlayer Coupling in Multilayer Graphene Field-Effect Transistors. *Nano Letters* **9** (8), 2973–2977 (2009). [11](#)
- [45] Žutić, I., Fabian, J. & Das Sarma, S. Spintronics: Fundamentals and applications. *Rev. Mod. Phys.* **76**, 323–410 (2004). [12](#)

-
- [46] Kuga, S.-i., Murakami, S. & Nagaosa, N. Spin hall effect of excitons. *Phys. Rev. B* **78**, 205201 (2008). [12](#)
- [47] Valenzuela, S. O. & Tinkham, M. Direct electronic measurement of the spin hall effect. *Nature* **442**, 176–179 (2006). [12](#)
- [48] Aronov, A. & Pikus, G. Spin Injection into Semiconductors. *Soviet Physics Semiconductors* **10**, 698 (1976). [12](#)
- [49] Jedema, F. *Electrical spin injection in metallic mesoscopic spin valves*. Ph.D. thesis, Zernike Institute of Advanced Materials (2002). [17](#)
- [50] Wikipedia. Four-terminal sensing — Wikipedia, The Free Encyclopedia (2010). [Online; accessed 02-July-2010]. [29](#)
- [51] Novoselov, K. S. *et al.* Electric Field Effect in Atomically Thin Carbon Films. *Science* **306**, 666–669 (2004). [29](#)
- [52] Bournalon, B., Miko, C., Forró, L., Glattli, D. C. & Bachtold, A. Intershell transport in multiwall carbon nanotubes. vol. 786, 544–547 (American Institute of Physics, 2005). [33](#)
- [53] Hwang, E. H., Adam, S. & Das Sarma, S. Carrier transport in two-dimensional graphene layers. *Phys. Rev. Lett.* **98**, 186806 (2007). [38](#)
- [54] Stauber, T., Peres, N. M. R. & Guinea, F. Electronic transport in graphene: A semiclassical approach including midgap states. *Phys. Rev. B* **76**, 205423 (2007). [38](#)
- [55] Chen, J.-H. *et al.* Charged-impurity scattering in graphene. *Nat Phys* **4**, 377–381 (2008). [38](#)